International Journal of Solids and Structures 83 (2016) 154–168

Contents lists available at ScienceDirect

International Journal of Solids and Structures

journal homepage: www.elsevier.com/locate/ijsolstr

Shear properties of heterogeneous fluid-filled porous media with spherical inclusions

Yongjia Song[a,*], Hengshan Hu[a], John W. Rudnicki[b]

[a] Department of Astronautics and Mechanics, Harbin Institute of Technology, P. O. Box 344, Harbin 150001, P R China
[b] Department of Civil and Environmental Engineering and Department of Mechanical Engineering, Northwestern University, Evanston, IL 60208, USA

ARTICLE INFO

Article history:
Received 26 March 2015
Revised 4 September 2015
Available online 23 January 2016

Keywords:
Porous medium
Wave-induced fluid flow
Effective shear modulus
Attenuation
Velocity dispersion

ABSTRACT

An exact analytical solution is presented for the effective dynamic shear modulus in a heterogeneous fluid-filled poroelastic medium containing spherical inclusions. The complex and frequency-dependent properties of the derived shear modulus are solely caused by the physical mechanism of mesoscopic-scale wave-induced fluid flow whose scale is assumed to be smaller than wavelength but larger than the size of pores. Our model consists of three phases: a spherical inclusion, a shell of matrix material with different mechanical and/or hydraulic properties and an outer region of effective homogeneous medium of infinite extent. This three-phase model represents a self-consistent model or an approximate model of composite having periodically distributed inclusions. The behaviors of both the inclusion and the matrix are described by Biot's equations (1941) with standard conditions of Deresiewicz and Skalak (1963) at the inclusion-matrix interface. The effective medium is regarded as an equivalent elastic or viscoelastic material with complex and frequency-dependent moduli to be determined. The derived effective shear modulus is used to quantify the shear-wave attenuation and velocity dispersion. For the problem of fluid patchy saturation (inclusions with the same solid frame as the matrix but with a different pore fluid from that in the matrix), the gas pocket does not affect the shear attenuation and dispersion characteristic of the water-filled matrix medium at all. For the problem of double porosity structure (inclusions having a different solid frame than the matrix but the same pore fluid as the matrix), with the increase of frequency the heterogeneous medium transitions from a low-frequency state having drained inclusions and drained matrix with no pore pressure difference to a higher-frequency state having undrained inclusions and undrained matrix with no fluid communication at the inclusion's surface. The relaxation frequency at which the maximum value of inverse quality factor occurs moves to frequencies by two orders of magnitude lower if the size of a unit cell increases by one order of magnitude. Stiff inclusions imbedded in a relatively soft matrix can cause significant and observable attenuation at seismic frequency bands, but softer inclusions imbedded in a relatively stiff matrix cause very weak attenuation. The mixed heterogeneity in both the solid frame and pore fluid also has important influences on the frequency-dependent shear wave attenuation.

© 2016 Elsevier Ltd. All rights reserved.

1. Introduction

The problems of velocity dispersion and attenuation of seismic waves in fluid-filled heterogeneous porous media have been of long-standing interest (e.g., Biot, 1956a,b; White, 1975; Dutta and Odé, 1979a,b; Berryman, 1985; Dvorkin, 1995; Pride and Berryman, 2003a; Müller et al., 2010; Song and Hu, 2013) with significant application in seismic exploration (e.g., Berryman et al. 2002; Ba et al., 2013) and acoustic well logging (e.g., Tang et al., 2012; Markova et al., 2014).

Earth crustal rocks are heterogeneous in various scales. Mesoscopic-scale wave-induced fluid flow (WIFF, Pride et al., 2004) whose scale is smaller than wavelength but larger than the size of pores generates heats and is believed to be the major physical mechanism in causing the intrinsic attenuation and velocity dispersion in seismic band of frequencies ($1 - 10^4$Hz) (Pride et al., 2004; Müller et al., 2010; Tisato and Quintal, 2013). From the body wave speed formula, it is well known that shear modulus not only critically determines the properties of the shear (S) wave but is significantly affects the properties of compressional (P) wave. Some

* Corresponding author.
E-mail addresses: songyongjia061220110@126.com (Y. Song), hhs@hit.edu.cn (H. Hu), john.rudnicki@gmail.com (J.W. Rudnicki).

http://dx.doi.org/10.1016/j.ijsolstr.2016.01.009
0020-7683/© 2016 Elsevier Ltd. All rights reserved.

experiments (Sams et al, 1997; Jones, 1986) show that the dispersion and attenuation of S waves could be of the same order of magnitude as those of P waves in fluid-saturated porous rocks. The present paper is devoted to study the effective shear properties in heterogeneous fluid-filled porous media by concerning mesoscopic WIFF.

Patchy saturation (inclusions having the same solid frame as the matrix but with a different pore fluid from the matrix) and double porosity (inclusions having a different solid frame than the matrix but the same pore fluid as the matrix) are two major models for seismic attenuation due to mesoscopic WIFF. Pride et al. (2004) showed that the heterogeneity in either the fluid or the solid frame can cause significant P-wave attenuation (maximum value of the inverse quality factor commonly lies in the range 0.01–0.1) in the seismic band of frequencies. To interpret the seismic attenuation and dispersion in heterogeneous porous rocks consisting of multiphase fluids and heterogeneous solids due to mesoscopic WIFF in porous rocks, many analytical solutions have been derived to quantify the dynamic bulk modulus and the attenuation in P waves (e.g., White, 1975; White et al, 1975; Dutta and Odé, 1979a,b; Berryman, 1985; Norris, 1993; Johnson, 2001; Pride and Berryman, 2003a; Pride et al., 2004; Müller and Gurevich, 2004; Brajanovski et al. 2005; Vogelaar and Smeulders, 2007; Vogelaar et al., 2010). For example, for consideration of energy loss in a patchy saturation reservoir rock, White (1975) derived the frequency-dependent effective bulk modulus by using a spherical gas-oil or gas-water pocket model. In his model, a small amount of gas in a fluid-saturated porous medium can cause significant velocity dispersion and attenuation in P waves (Dutta and Odé,1979a,b; Johnson, 2001; Pride et al., 2004; Vogelaar et al., 2010). Dutta and Odé (1979a,b) and Vogelaar et al. (2010) solved the problem exactly using the Biot consolidation theory of quasi-static poroelasticity and confirmed White's results. In addition, White (1975) suggested that the effective shear modulus is identical to the dry shear modulus of the porous composite because physically the fluid filling the pores changes neither the shear force existing in the solid frame nor the shear modulus. Pride and Berryman (2003a,b) developed double porosity theory to model acoustic propagation through heterogeneous porous structures with two different porous frames. Since the sphere is one of several typical and simple geometric inclusions, and is also a special case of the ellipsoid, it has been used to interpret the intrinsic P-wave attenuation in porous fluid-filled rocks. In addition to White's spherical-inclusion patchy model (White, 1975), Ba et al. (2011) considered a double-porosity medium consisting of spherical inclusions imbedded in an unbounded matrix having different porosity, permeability and compressibility. They derived the equations of motion showing that the spherical inclusion can cause significant fast P wave (which is similar to the ordinary P wave in elastic medium but has intrinsic energy loss in the propagation process) attenuation and dispersion in the seismic frequency band.

However, unlike the case of effective bulk modulus, deriving the effective shear modulus is rather complicated as it involves solving the shear deformation of phases. Recently, several papers have considered the shear properties in poroelastic media. For example, Berryman (2004) studied the dependence of macroscopic shear modulus on pore-fluid properties by using a locally isotropic layered model. He gave upper and lower bounds under drained and undrained boundary conditions, respectively. Masson and Pride (2007) estimated by finite difference modeling the shear attenuation and shear modulus dispersion in a double porosity model in which a soft porous ellipsoid is embedded within a stiffer matrix. They showed that significant attenuation over the seismic frequency range occurs as for P waves but smaller in magnitude. Quintal et al. (2012) used the finite-element method to model the S-wave modulus and attenuation in a 2-dimensional patchy saturation structure. They showed that the role of S-wave attenuation could be used as an indicator of fluid content in a reservoir in addition to P-wave attenuation. Other numerical methods studying the attenuation in shear waves can be found in Rubino et al. (2008), Wenzlau et al. (2010), Quintal et al. (2011) and Masson and Pride (2014). Liu et al. (2009) derived a series expansion solution for the scattering of incident S waves by mesoscopic-scale spherical inclusions embedded in an infinite poroelastic matrix. After obtaining the series expansion solution, they used a dilute model to calculate the scattering S-wave dispersion and attenuation. Significant S-wave attenuation is caused in the double porosity model at an S-wave wavelength that is approximately equal to the characteristic size of the inclusion. Although these papers above focus on the S-wave attenuation due to mesoscopic WIFF, unfortunately, to the best of our knowledge, no analytical solution for dynamic effective shear modulus in any typical structure has been given to account for the role of the mechanism of mesoscopic WIFF.

It is worth mentioning that the scattering approach is indeed a powerful tool to study the attenuation and velocity dispersion in heterogeneous porous media. As pointed out by Müller and Gurevich (2005), the processes of wave conversion scattering into Biot's slow P waves is equivalent to the mechanism of pore pressure relaxation due to wave-induced perturbation and thus also describes the mechanism of WIFF. An important application of the scattered Biot's slow P wave is to analyze the effective properties, attenuation and velocity dispersion of elastic waves in poroelastic materials. Berryman (1985) first analyzed the scattering of incident P wave by a porous spherical inclusion in an otherwise homogeneous porous matrix medium. One major difficulty is that the solution is given in terms of an infinite series, and one needs to solve a 6×6 system of equations for the coefficients at each harmonic. The analytical solution can be obtained only after some simplifications (e.g., Berryman, 1985; Ciz and Gurevich; 2005). Berryman (1985) obtained the asymptotic long-wavelength solution for the slow wave amplitude, which is valid for inclusions much smaller than the wavelength of Biot's slow wave. Ciz and Gurevich (2005) analyzed the amplitude of the Biot's slow wave for the scattering of incident P waves by spherical inclusions in the low-frequency variant of Biot's theory, and for the inclusion size much smaller than the wavelength of the fast P wave. A simple expression for the amplitude of the scattered Biot's slow wave was obtained by assuming that the amplitude of the scattered fast compressional wave is well approximated by the solution of the equivalent elastic problem. Ciz et al. (2006) applied Waterman–Truell multiple scattering theory to relate the scattering of a single inclusion to the wave attenuation in the poroelastic medium. Gurevich et al. (1998) applied the Born approximation to study the scattering of a fast P wave in a poroelastic medium by an ellipsoidal inclusion. The Born approximation is valid for low contrast of the inclusion's properties with respect to the matrix medium.

This paper focuses on dynamic effective shear modulus. The limitation of this paper is that the size of a unit cell shown in Fig. 1 is smaller than S-wave wavelength and much larger than the size of pores. Biot's equations for consolidation (Biot, 1941) of poroelastic media are employed to study the effective shear modulus for a heterogeneous medium containing spherical inclusions. The dispersive shear modulus is due to the heterogeneous distribution of pore fluid pressure and pore pressure diffusion. Furthermore, because no inertia terms appear in the equations for consolidation, the attenuation is solely due to flow of the viscous fluid, which is controlled by the gradient of the pore-fluid pressure. Excluding the inertial forces at low seismic frequencies is a valid approximation because they are negligible for typical properties of rocks and saturating fluids at these frequencies (e.g., Bourbie et al., 1987). The present work presents an analytical solution for the dynamic shear modulus of a heterogeneous poroelastic material containing

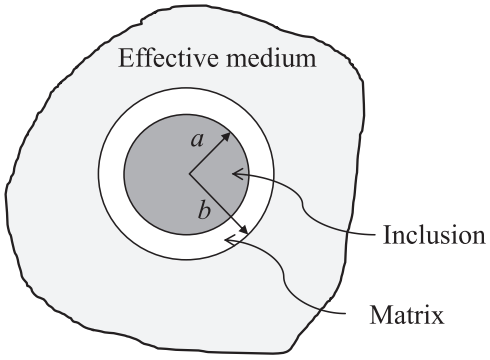

Fig. 1. Three-phase model.

mesoscopic-scale spherical inclusions. (The problem of a spherical cavity which is embedded in a linear, fluid-filled, elastic porous medium and which is subjected to the sudden quasi-static application of a stress at the cavity boundary is solved by Rice et al. (1978).)

The present paper is organized as follows. To quantify the effective shear properties, a three-phase model of poroelasticity and Biot's theory of quasi-static poroelasticity (Biot, 1941) are introduced and briefly reviewed. Christensen and Lo (1979) presented a three-phase model of elasticity to study the effective shear modulus in a classic elasticity composite. We extend their model to the case of poroelasticity. Then we solve the Biot's governing equations with standard interface continuity conditions of Deresiewicz and Skalak (1963) and obtain the effective shear modulus. Next, we calculate the S-wave attenuation and dispersion. Finally, the conclusions are summarized.

2. Three-phase model and Biot's theory

2.1. Three-phase model of poroelasticity

To obtain the effective shear moduli, a geometric model of the composite must be given at first. The corresponding model employed in this article is shown in Fig. 1. It involves three phases: a spherical isotropic inclusion with radius of a, a shell of isotropic matrix with thickness of $b-a$ and an outer region of effective homogeneous medium of infinite extent. We use Biot's theory of quasi-static poroelasticity to describe the mechanical and hydraulic behaviors of both the inclusion and matrix. The inclusion has different physical properties, which include solid frame and/or pore fluid, from the matrix. As is shown in Fig. 1, an inclusion and its surrounding matrix shell consist of a spherical unit cell, which is imbedded in an unbounded equivalent medium.

Let the unit cell be equivalent by the outer homogeneous medium whose properties are yet to be determined. An ideal material for the outer effective medium is likely to be a poroelastic medium as well. But, since the present paper discusses the effective shear modulus of the unit cell only, for simplicity, we assume that the outer homogeneous medium can be equivalent by an effective elastic or viscoelastic material with unknown shear modulus.

The idea of the three-phase model is first presented by Christensen and Lo (1979). They use this model to analyze the effective shear modulus in an ordinary elastic composite. This study extends their three-phase model to the case of poroelasticity. Since the three-phase model assumes that the composite sphere is embedded in an effective medium whose properties are to be determined, this is very similar to the self-consistent method, thus the three-phase model is also called a generalized self-consistent model by others (e.g., Qu and Cherkaoui, 2006). White (1975) used a very similar geometric model to analyze the P-wave attenuation in a patchy saturation reservoir in which he suggested the gas pockets are periodically distributed within the water-saturated porous matrix. The geometric structure shown in Fig. 1 will be used to determine the effective shear modulus in Section 3. Before doing this, we briefly review the governing equations of Biot's theory.

2.2. Biot's theory of quasi-static poroelasticity

It is assumed that the size of a spherical unit cell in the present three-phase model is smaller than S-wave wavelength. To study the effects of mesoscopic-scale WIFF on shear properties, Biot's theory of poroelasticity (Biot, 1941) is exploited to describe the behaviors of the inclusion and matrix. Inertial effects are neglected and the attenuation is solely due to flow of the viscous fluid, which is controlled by the gradient of the pore-fluid pressure. Rudnicki (1986) presented Biot's governing equations in the displacement-mass ($u_p-\Delta m$) formulation in which the fluid mass diffusion is decoupled from frame deformation. We follow Rudnicki's treatment. The coupled poroelastic behavior of solid frame deformation $u_{p,q}(=\partial u_p/\partial x_q)$, the displacement gradient and change in m, the fluid mass content per unit reference volume of porous solid, are related to the total stress σ_{pq} and pore fluid pressure p_f via the following constitutive equations

$$\sigma_{pq}=\mu(u_{p,q}+u_{q,p})+\lambda u_{k,k}\delta_{pq}-\alpha p_f\delta_{pq}, \tag{1}$$

$$\Delta m=m-m_0=\alpha\rho_f\left[u_{k,k}+\alpha p_f/(\lambda_u-\lambda)\right], \tag{2}$$

where m_0 is the reference value of m, ρ_f is the mass density of pore fluid and δ_{pq} is the Kronecker delta. λ and $\mu$are the Lamé moduli appropriate for drained or dry response, whereas λ_u is the Lamé modulus for undrained response. $\alpha=1-K/K_s$ is the Biot coefficient, $K(=\lambda+2\mu/3)$ is the drained bulk modulus and K_s is the bulk modulus of the solid constituents. λ_u is related to λ by $\lambda_u=\lambda+\alpha^2M$, where$M=1/[\phi/K_f+(\alpha-\phi)/K_s]$, K_f is the fluid bulk modulus and ϕ is the porosity.

The constitutive formulation is completed by Darcy's law which, in the absence of body force, is given by

$$q_p=-\rho_f\gamma\,\partial p_f/\partial x_p, \tag{3}$$

where $q_p(=\rho_f\partial w_p/\partial t)$ is the mass flow rate per unit area in the x_p direction and w_p is the filtration displacement. γ is related to κ, the permeability and η, the fluid viscosity by $\gamma=\kappa/\eta$. Darcy's law describes a quasi-static flow in pores.

Substituting Eq. (1) into the equilibrium equation $\sigma_{pq,p}=0$ and eliminating p_f by using Eq. (2) yield

$$(\lambda_u+\mu)u_{k,kp}+\mu u_{p,kk}=(\lambda_u-\lambda)\left(\alpha\rho_f\right)^{-1}(\Delta m)_{,p}. \tag{4}$$

Eq. (4) shows that the deformation is coupled with fluid filtration and that a porous material behaves as an otherwise undrained medium with the gradient of change in fluid mass acting as a body force.

Substituting Darcy's law (3) into $q_{k,k}+\partial m/\partial t=0$, the equation of fluid mass conservation without fluid mass source, and using Eq. (2) and the divergence of Eq. (4) lead to a diffusion equation for Δm:

$$\partial(\Delta m)/\partial t=c\nabla^2(\Delta m), \tag{5}$$

where the diffusivity is

$$c=\frac{\gamma(\lambda_u-\lambda)(\lambda+2\mu)}{\alpha^2(\lambda_u+2\mu)}, \tag{6}$$

and $\nabla^2=\frac{\partial^2}{\partial x_k\partial x_k}$.

In the following section we will use the governing Eqs. (1)–(5) to derive solutions for the effective viscoelastic (complex and frequency-dependent) shear modulus in the three-phase model.

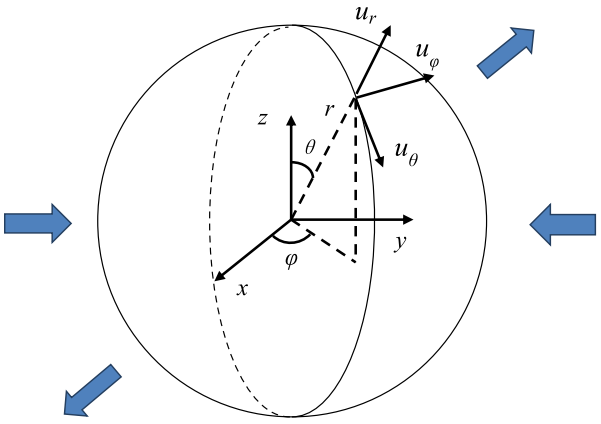

Fig. 2. Displacement components and applied shear loadings in the coordinate system. The arrows show the pure shear loading in the far field, with a tensile stress in the x-direction and a compressional stress of the same magnitude in the y-direction.

3. Effective shear modulus

3.1. Expressions of displacement, stress and pore pressure

Introduce a spherical coordinate system with the origin at the center of the spherical unit cell shown in Fig. 1. The two radii in Fig. 1 are taken such that $a^3/b^3 = \beta$, the volume fraction of the inclusion. To determine the shear properties in such a poroelastic composite, let the three-phase specimen be subjected to pure shear loadings in the x-y plane at infinity with tension in x direction and compression in y direction. Fig. 2 shows a schematic diagram of displacement components and the pure shear loadings in the coordinate system. Suitable displacement components and Δm have the form

$$u_r = U_r \sin^2\theta \cos 2\varphi, \tag{7}$$

$$u_\theta = U_\theta \sin\theta \cos\theta \cos 2\varphi, \tag{8}$$

$$u_\varphi = -U_\theta \sin\theta \sin 2\varphi, \tag{9}$$

$$\Delta m = \Delta M \sin^2\theta \cos 2\varphi, \tag{10}$$

where U_r, U_θ and ΔM are functions of r only. r, θ and φ are the spherical polar coordinates shown in Fig. 2. The form of the displacements in (7)-(9) has been used by Christensen and Lo (1979) to calculate the effective shear modulus in an ordinary elastic composite. With the expectation that the displacement solutions will involve the same spherical forms which appeared in the corresponding problem of classic elasticity, Eqs. (7)–(9) is also used to describe shear displacements in a poroelastic medium. Moreover, since considerations of symmetry and linearity also indicate that Δm has the same form with respect to angle coordinates as radial displacement u_r, Eq. (10) is needed to account for the coupled poroelastic effect. Based on the uniqueness theorem in poroelasticity (Deresiewicz and Skalak, 1963), the forms of Eqs. (7)–(10) will be suitable as long as one is able to succeed in finding the solutions for this shear problem.

Adopting an $e^{-i\omega t}$ dependence and substituting Eq. (10) into the fluid mass diffusion Eq. (5) leads to the general form of ΔM by (see the derivation in Appendix A)

$$\Delta M(r) = E j_2(kr) + F n_2(kr). \tag{11}$$

where $\partial/\partial t = -i\omega$ is used, j_2 and n_2 are the 2nd-order spherical Bessel functions of the first and second kinds, $k = \sqrt{i\omega/c}$ is of the dimension of wave number, and ω is the angle frequency. Coefficients E and F are to be determined by boundary conditions.

Substituting Eqs. (7)–(11) into the equilibrium Eq. (4) allows us solve for the displacement components U_r and U_θ. The expressions for U_r and U_θ are

$$U_r = Ar - \frac{2\nu_u}{1-2\nu_u} Br^3 + \frac{5-4\nu_u}{2(1-2\nu_u)} \frac{C}{r^2} + \frac{D}{r^4} + \frac{\chi}{10k}\{E[3j_3(kr) - 2j_1(kr)] + F[3n_3(kr) - 2n_1(kr)]\}. \tag{12}$$

$$U_\theta = Ar - \frac{7-4\nu_u}{3(1-2\nu_u)} Br^3 + \frac{C}{r^2} - \frac{2}{3}\frac{D}{r^4} - \frac{\chi}{5k}\{E[j_1(kr) + j_3(kr)] + F[n_1(kr) + n_3(kr)]\}. \tag{13}$$

where $\nu_u (= \frac{3K_u - 2\mu}{6K_u + 2\mu})$ is the Poisson ratio for undrained response and $\chi = 2\frac{\lambda_u - \lambda}{\alpha H \rho_f}$, and $H (= \lambda_u + 2\mu = \frac{2\mu(1-\nu_u)}{1-2\nu_u})$ is the P-wave modulus defined by Biot (1962). The derivation of Eq. (12) is shown in Appendix A. The expressions for U_r and U_θ have two parts. The first part which has terms of r, r^3, r^{-2} and r^{-4} with undrained Poisson ratio is identical to the form of the solution for an ordinary elastic material (see Christensen and Lo, 1979). The second part, which consists of spherical Bessel functions, is generated by fluid flow. The above equations are general and apply to both inclusion and shell. Unlike the series-expansion solution given by scattering approach (Berryman, 1985; Liu et al., 2009), in which the solution is appropriate even for wavelength smaller than the inclusion, the above equations are valid only for long wavelengths. Eqs. (7)–(13) are appropriate for the unit cell size smaller than the shear wavelength λ_s, i.e., $b << \lambda_s (= \omega^{-1} V_s)$ where V_s is the S-wave velocity. Note that the diffusion length $d = \sqrt{c/\omega}$ is also smaller than shear wavelength λ_s within seismic frequencies for typical poroelastic rocks. The frequency-dependent characteristics investigated in this paper are solely due to the fluid diffusion effect.

Now, substituting Eqs. (11)–(13) into Eqs. (7) and (10), and then substituting the results into the constitutive equations yield stresses, pore pressure and filtration displacement:

$$\sigma_{rr} = \Sigma_r(r)\sin^2\theta \cos 2\varphi \tag{14}$$

$$\sigma_{r\theta} = \Sigma_\theta(r) \sin\theta \cos\theta \cos 2\varphi \tag{15}$$

$$p_f = P_f(r)\sin^2\theta \cos 2\varphi \tag{16}$$

$$w_r = W_r(r)\sin^2\theta \cos 2\varphi \tag{17}$$

where

$$\Sigma_r(r) = 2\mu A + \frac{2\mu\nu_u}{1-2\nu_u} Br^2 + \frac{2\mu(\nu_u - 5)}{1-2\nu_u}\frac{C}{r^3} - 8\mu\frac{D}{r^5} - \frac{2}{5}\mu\chi E\left[\frac{1}{3}j_0(kr) + \frac{25}{21}j_2(kr) + \frac{6}{7}j_4(kr)\right] - \frac{2}{5}\mu\chi F\left[\frac{1}{3}n_0(kr) + \frac{25}{21}n_2(kr) + \frac{6}{7}n_4(kr)\right] \tag{18}$$

$$\Sigma_\theta(r) = 2\mu A - \frac{2\mu(7+2\nu_u)}{3(1-2\nu_u)} Br^2 + \frac{2\mu(1+\nu_u)}{1-2\nu_u}\frac{C}{r^3} + \frac{16}{3}\frac{\mu D}{r^5} - \frac{2}{5}\mu\chi E\left[\frac{1}{3}j_0(kr) - \frac{5}{21}j_2(kr) - \frac{4}{7}j_4(kr)\right] - \frac{2}{5}\mu\chi F\left[\frac{1}{3}n_0(kr) - \frac{5}{21}n_2(kr) - \frac{4}{7}n_4(kr)\right] \tag{19}$$

$$P_f(r) = \frac{\lambda_u - \lambda}{\alpha}\left(-7Br^2 + 3\frac{C}{r^3}\right) + \frac{\chi}{2\alpha}H_d[Ej_2(kr) + Fn_2(kr)] \tag{20}$$

$$W_r(r) = \frac{i\gamma}{\alpha\omega}(\lambda_u - \lambda)\left(14Br + 9\frac{C}{r^4}\right) - \frac{ik\gamma\chi H_d}{10\alpha\omega}E[2j_1(kr) - 3j_3(kr)] - \frac{ik\gamma\chi H_d}{10\alpha\omega}F[2n_1(kr) - 3n_3(kr)] \quad (21)$$

and where $H_d(=\lambda+2\mu)$ is the drained P-wave modulus. σ_{rr} is the normal stress in the radial direction. $\sigma_{r\theta}$ is the shear stress. w_r is the radial filtration displacement.

3.2. Exact analytical solution

As seen in Fig. 1, there are three separate regions in which the solutions must be known. Let subscripts *i*, *m* and *e* denote the inclusion, the matrix and the outer effective medium, respectively. The coefficients C_i, D_i and F_i in the inclusion must be zero in order for the poroelastic solutions at $r = 0$ to be finite. Moreover, the effective elastic or viscoelastic assumption and the requirement that the solutions at $r = \infty$ must be finite imply $B_e = E_e = F_e = 0$ in the effective medium region. Furthermore, Christensen and Lo (1979) show that

$$C_e = 0 \quad (22)$$

for the three-phase model by Eshelby interaction energy approach. Although they obtain this result in an ordinary elastic composite, this result is appropriately used in the outer equivalent homogeneous elastic or viscoelastic medium in the present study.

Now, the general forms of poroelastic and elastic solutions in the three separate regions of Fig. 1 are given by

$$U_{ri} = A_i r - \frac{2\nu_{ui}}{1-2\nu_{ui}}B_i r^3 + \frac{\chi_i}{10k_i}E_i[3j_3(k_i r) - 2j_1(k_i r)] \quad (23)$$

$$U_{\theta i} = A_i r - \frac{7-4\nu_{ui}}{3(1-2\nu_{ui})}B_i r^3 - \frac{\chi_i}{5k_i}E_i[j_1(k_i r) + j_3(k_i r)] \quad (24)$$

$$\Sigma_{ri} = 2\mu_i A_i + \frac{2\mu_i\nu_{ui}}{1-2\nu_{ui}}B_i r^2 - 2\mu_i\chi_i E_i\left[\frac{1}{15}j_0(k_i r) + \frac{5}{21}j_2(k_i r) + \frac{6}{35}j_4(k_i r)\right] \quad (25)$$

$$\Sigma_{\theta i} = 2\mu_i A_i - \frac{2\mu_i(7+2\nu_{ui})}{3(1-2\nu_{ui})}B_i r^2 - 2\mu_i\chi_i E_i\left[\frac{1}{15}j_0(k_i r) - \frac{1}{21}j_2(k_i r) - \frac{4}{35}j_4(k_i r)\right] \quad (26)$$

$$P_{fi} = -7\frac{\lambda_{ui}-\lambda_i}{\alpha_i}B_i r^2 + \frac{\chi_i}{2\alpha_i}H_{di}E_i j_2(k_i r) \quad (27)$$

$$W_{ri} = \frac{14i\gamma_i}{\alpha_i\omega}(\lambda_{ui}-\lambda_i)B_i r - \frac{ik_i\gamma_i\chi_i H_{di}}{10\alpha_i\omega}E_i[2j_1(k_i r) - 3j_3(k_i r)] \quad (28)$$

in the inclusion,

$$U_{rm} = A_m r - \frac{2\nu_{um}}{1-2\nu_{um}}B_m r^3 + \frac{5-4\nu_{um}}{2(1-2\nu_{um})}\frac{C_m}{r^2} + \frac{D_m}{r^4} + \frac{\chi_m}{10k_m}\{E_m[3j_3(k_m r) - 2j_1(k_m r)] + F_m[3n_3(k_m r) - 2n_1(k_m r)]\} \quad (29)$$

$$U_{\theta m} = A_m r - \frac{7-4\nu_{um}}{3(1-2\nu_{um})}B_m r^3 + \frac{C_m}{r^2} - \frac{2}{3}\frac{D_m}{r^4} - \frac{\chi_m}{5k_m}\{E_m[j_1(k_m r) + j_3(k_m r)] + F_m[n_1(k_m r) + n_3(k_m r)]\} \quad (30)$$

$$\Sigma_{rm} = 2\mu_m A_m + \frac{2\mu_m\nu_{um}}{1-2\nu_{um}}B_m r^2 + \frac{2\mu_m(\nu_{um}-5)}{1-2\nu_{um}}\frac{C_m}{r^3} - 8\mu_m\frac{D_m}{r^5} - 2\mu_m\chi_m E_m\left[\frac{1}{15}j_0(k_m r) + \frac{5}{21}j_2(k_m r) + \frac{6}{35}j_4(k_m r)\right] - 2\mu_m\chi_m F_m\left[\frac{1}{15}n_0(k_m r) + \frac{5}{21}n_2(k_m r) + \frac{6}{35}n_4(k_m r)\right] \quad (31)$$

$$\Sigma_{\theta m} = 2\mu_m A_m - \frac{2\mu_m(7+2\nu_{um})}{3(1-2\nu_{um})}B_m r^2 + \frac{2\mu_m(1+\nu_{um})}{1-2\nu_{um}}\frac{C_m}{r^3} + \frac{16}{3}\frac{\mu_m D_m}{r^5} - 2\mu_m\chi_m E_m\left[\frac{1}{15}j_0(k_m r) - \frac{1}{21}j_2(k_m r) - \frac{4}{35}j_4(k_m r)\right] - 2\mu_m\chi_m F_m\left[\frac{1}{15}n_0(k_m r) - \frac{1}{21}n_2(k_m r) - \frac{4}{35}n_4(k_m r)\right] \quad (32)$$

$$P_{fm} = \frac{\lambda_{um}-\lambda_m}{\alpha_m}\left(-7B_m r^2 + 3\frac{C_m}{r^3}\right) + \frac{\chi_m}{2\alpha_m}H_{dm}[E_m j_2(k_m r) + F_m n_2(k_m r)] \quad (33)$$

$$W_{rm} = \frac{i\gamma_m}{\alpha_m\omega}(\lambda_{um}-\lambda_m)\left(14B_m r + 9\frac{C_m}{r^4}\right) - \frac{ik_m\gamma_m\chi_m H_{dm}}{10\alpha_m\omega}E_m[2j_1(k_m r) - 3j_3(k_m r)] - \frac{ik_m\gamma_m\chi_m H_{dm}}{10\alpha_m\omega}F_m[2n_1(k_m r) - 3n_3(k_m r)] \quad (34)$$

in the matrix, and

$$U_{re} = A_e r + \frac{D_e}{r^4} \quad (35)$$

$$U_{\theta e} = A_e r - \frac{2}{3}\frac{D_e}{r^4} \quad (36)$$

$$\Sigma_{re} = 2\mu_e A_e - 8\frac{\mu_e D_e}{r^5} \quad (37)$$

$$\Sigma_{\theta e} = 2\mu_e A_e + \frac{16}{3}\frac{\mu_e D_e}{r^5} \quad (38)$$

in the effective medium, where k_i and k_m are wave numbers in the inclusion and matrix, respectively. ν_{ui} and ν_{um} are the undrained Poisson ratios of the inclusion and the matrix, respectively. μ_i and μ_m are the shear moduli of the inclusion and the matrix, respectively.μ_e is the effective shear modulus to be determined. $H_{di}(=\lambda_i+2\mu_i)$ and $H_{dm}(=\lambda_m+2\mu_m)$ are drained P-wave moduli of the inclusion and the matrix, respectively. In these equations, A_i, B_i, E_i, A_m, B_m, C_m, D_m, E_m, F_m, A_e and D_e are coefficients to be determined from the boundary conditions at the inclusion-matrix and matrix-effective interfaces.

We use the interface conditions given by Deresiewicz and Skalak (1963) to describe the physical continuity at inclusion-matrix interface. At the inclusion-matrix interface ($r = a$), six independent continuity conditions involve the continuity of the displacements u_r and u_θ, the stresses σ_{rr}, $\sigma_{r\theta}$, the pore pressure p_f and the radial filtration displacement w_r. These six continuity conditions lead to the following equations sequentially:

$$U_{ri}(a) = U_{rm}(a) \quad (39)$$

$$U_{\theta i}(a) = U_{\theta m}(a) \quad (40)$$

$$\Sigma_{ri}(a) = \Sigma_{rm}(a) \quad (41)$$

$$\Sigma_{\theta i}(a) = \Sigma_{\theta m}(a) \tag{42}$$

$$P_{fi}(a) = P_{fm}(a) \tag{43}$$

$$W_{ri}(a) = W_{rm}(a) \tag{44}$$

We need to point out that the above boundary conditions are based on the assumption of perfect contact between the contiguous porous media. The boundary conditions are by no means unique. For example, Eq. (43) can be replaced by a pressure jump boundary condition

$$p_{fi} - p_{fm} = Lw_r$$

where L is the interface flow impedance. This equation can be used to quantify effects of capillary forces and/or imperfect hydraulic contacts on attenuation and dispersion (Nagy and Blano, 1994; Qi et al, 2014a; Gurevich and Schoenberg, 1999; Qi et al., 2014b). However, the present paper aims at discussing the effect of mesoscopic-scale WIFF on wave attenuation. Therefore, the interface flow impedance effect is neglected ($L = 0$).

Furthermore, at the interface between the matrix and the effective medium ($r = b$), four independent boundary conditions involve the continuity of the displacements u_r and u_θ and stresses σ_{rr} and $\sigma_{r\theta}$. The continuity of u_r, u_θ, σ_{rr}, $\sigma_{r\theta}$ at $r = b$ gives the following equations sequentially:

$$U_{rm}(b) = U_{re}(b) \tag{45}$$

$$U_{\theta m}(b) = U_{\theta e}(b) \tag{46}$$

$$\Sigma_{rm}(b) = \Sigma_{re}(b) \tag{47}$$

$$\Sigma_{\theta m}(b) = \Sigma_{\theta e}(b) \tag{48}$$

Now, we have ten boundary conditions owing to the continuity at the two interfaces. To determine the eleven coefficients, one more boundary condition at $r = b$ is required. We need to point out that the fifth boundary condition at $r = b$ is an open issue. Next, we discuss two possible situations for the required boundary condition.

Situation 1. Open pore boundary condition: $p_f = 0$ at $r = b$.

For the present problem of poroelastic media with pure shear stress, the averaged pore fluid pressure vanishes. The purpose of introducing the outer effective medium is to estimate the average properties of the unit cell. The open pore condition means the pore fluid pressure along the effective medium surface is identical to the average value of the pore fluid pressure. This situation concerns the self-consistent characteristics of our three-phase model. The open pore condition at $r = b$ leads to

$$P_{fm}(b) = 0. \tag{49}$$

Situation 2. Sealed pore boundary condition: $w_r = 0$ at $r = b$.

Recall that we have assumed the outer effective medium to be an equivalent viscoelastic solid. The sealed pore condition means that there is no fluid mass flowing across the interface between the poroelastic matrix and the effective solid. This situation describes an actual impermeable state at the pore-solid interface. The sealed pore condition at $r = b$ leads to

$$W_{rm}(b) = 0. \tag{49′}$$

White (1975); Dutta and Odé (1979a,b) and Vogelaar et al. (2010) used this sealed pore boundary condition to solve for the effective bulk modulus for a spherical patchy-saturation inclusion. We compare calculation examples for the two boundary situations in the next section.

To solve for the effective shear modulus, we use Eqs. (23)–(38) to rewrite Eqs. (39)–(49) in the matrix form as

$$\mathbf{ax} = 0\left(\text{or } \sum_{j=1}^{11} a_{ij}x_j = 0\right), \tag{50}$$

where **a**is a 11 × 11 matrix with complex elements, **x** is a column vector of eleven unknown coefficients (A_i, B_i, E_i, A_m, B_m, C_m, D_m, E_m, F_m, A_e and D_e). The objective is to find the effective shear modulus μ_e such that the determinant of matrix **a** is identical to zero ($|\mathbf{a}| = 0$). It is worth mentioning that the choice of **a** is not unique due to the properties of elementary transformation of matrix. Non-dimensional and concise choices of the elements of **a** are shown in Appendix B. Based on the elements shown in Appendix B, the equation for determining the effective shear modulus μ_e is

$$A_1\left(\frac{\mu_e}{\mu_m}\right)^2 + A_2\frac{\mu_e}{\mu_m} + A_3 = 0 \tag{51}$$

with

$$A_1 = 4a_{10,10;9,11}, \tag{52}$$

$$A_2 = 3a_{7,10;9,11} + a_{7,10;10,11} - 2a_{9,10;8,11} - 2a_{8,10;10,11}, \tag{53}$$

$$A_3 = -a_{8,10;7,11}, \tag{54}$$

where $a_{r,\,10;\,s,\,11}$ $(r, s = 7, 8, 9, 10)$ is the determinant of the 9 × 9 matrix generated from **a** by removing elements in rth and sth rows and in 10th and 11th columns.

Relation (51) is the final form sought. Using the quadratic formula

$$\frac{\mu_e}{\mu_m} = \frac{-A_2 \pm \sqrt{A_2^2 - 4A_1A_3}}{2A_1}, \tag{55}$$

we can determine the exact solution for effective shear modulus of the spherical model.

4. Calculation examples

The main purpose of this section is to quantify S-wave attenuation and velocity dispersion in media containing mesoscopic-scale heterogeneous solid frames and/or fluids. The S-wave phase velocity V_s and inverse quality factor Q^{-1} can be expressed as

$$V_s = \frac{1}{\mathrm{Re}\left(\sqrt{\rho/\mu_e}\right)} \tag{56}$$

$$Q^{-1} = 2\frac{\mathrm{Im}\left(\sqrt{\rho/\mu_e}\right)}{\mathrm{Re}\left(\sqrt{\rho/\mu_e}\right)} \tag{57}$$

where Re and Im denote the real and imaginary parts. $\rho = \beta\rho_i + (1-\beta)\rho_m$ is the effective density, where ρ_m and ρ_i are the bulk densities of matrix and inclusion, respectively. Use of Eqs. (52) and (55) and elements shown in Appendix B, and then substituting them into Eqs. (56) and (57) we can calculate the velocity dispersion and attenuation.

4.1. Parameters

To compute the S-wave attenuation and velocity dispersion one must specify the physical properties and geometric parameters of the inclusion and matrix. Material parameters of two kinds of rocks and three kinds of fluids listed in Tables 1 and 2 are used to construct the physical properties of the inclusion and matrix. The

Table 1
Physical properties of the rocks and fluids.

Parameter	Symbol	Rock 1	Rock 2
Drained bulk modulus	K (GPa)	13	0.13
Shear modulus	μ (GPa)	10	0.1
Solid bulk modulus	K_s (GPa)	38	38
Solid density	ρ_s (kg/m^3)	2650	2650
Porosity	ϕ	0.15	0.3
Permeability	κ (m^2)	1.3×10^{-13}	1.3×10^{-11}

Table 2
Physical properties of the fluids.

Parameter	Symbol	Water	Gas	Oil
Bulk modulus	K_f (GPa)	2.25	1.4×10^{-4}	1.4
Viscosity	η (Pa•s)	0.001	1.8×10^{-5}	0.02
Density	ρ_f (kg/m^3)	1000	1.3	880

two rocks shown in Table 1 differ by porosity, permeability and elastic properties. The drained stiffness (bulk and shear moduli) of the high porosity rock (rock 2) are only 1% of the low porosity rock (rock 1). Rock 2 represents a relatively softer porous solid, while rock 1 represents a stiffer porous solid. Physical parameters of water and gas given in Table 2 quantify the difference in pore fluids. The two rocks and the three fluids could be arbitrarily combined to determine the inclusion and matrix. Table 3 lists the material combinations and geometry parameters for inclusion and matrix.

4.2. Calculation result

Fig. 3 shows the dispersion curves of S-wave phase velocity (a) and inverse quality factor (b) for a double-porosity model with a fixed inclusion concentration $\beta = 0.2$ and unit cell radii of $b = 0.01, 0.1$ and 1m, respectively. In this double-porosity model, the matrix is the water-saturated rock 1 and the inclusion is the water-saturated rock 2 (Table 3). Results of the open pore situation and sealed pore situation are also compared in Fig. 3. The black lines and the blue lines represent results of open pore situation and sealed pore situation, respectively. It is shown that the velocity and attenuation curves in the open pore situation are very similar to the curves in the sealed pore situation. At first, we look at the similarities between the two distinct situations. All velocity curves show that the velocity at the high frequency limit is higher than that at the low frequency limit and the velocity increases with frequency. The velocity dispersion is caused entirely by the frequency-dependent effective shear modulus due to fluid flow because the density is unchanged. On the other hand, the frequency dependences of the velocity and the attenuation show that relaxation frequencies at which the maximum value of inverse quality factors occur move to lower frequencies by two orders of magnitude when the size of the unit cell increases by one order of magnitude. This is a feature similar to P waves (Pride et al., 2004; Ciz et al., 2006).

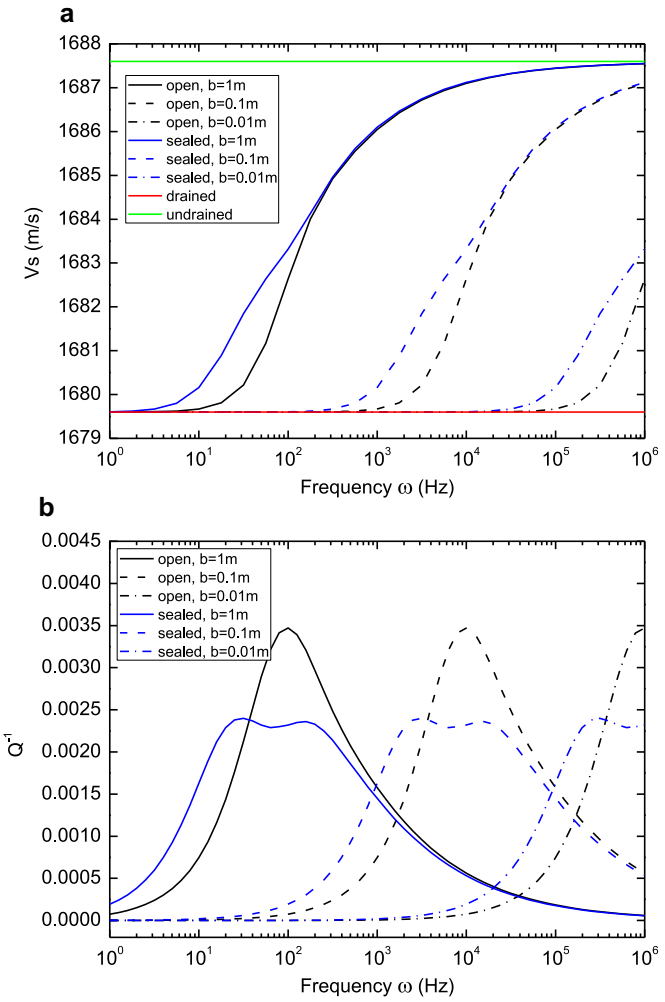

Fig. 3. S-wave phase velocity (a) and inverse quality factor (b) of a double-porosity model with a fixed inclusion concentration $\beta = 0.2$ but various radius $b = 0.01, 0.1$ and 1m. Black lines and blue lines are results for the open pore situation and sealed pore situation, respectively. The matrix is water-saturated rock 1, and the inclusion is water-saturated rock 2. The rock and fluid properties are given in Tables 1 and 2. The effective shear moduli in red and green lines in (a) are calculated by means of Christensen and Lo (1979) by using drained and undrained Poisson's ratios, respectively. (For interpretation of the references to color in this figure legend, the reader is referred to the web version of this article).

To get more physical insights on the lower-frequency and higher-frequency velocities, in Fig. 3(a) two curves of S-wave velocities (green and red lines) are calculated via the effective shear moduli by means of classic three-phase elasticity model (Christensen and Lo, 1979). The effective shear modulus in the elasticity model depends on the shear moduli, Poisson ratios of matrix and inclusion and the inclusion concentration. The detail

Table 3
Material choices and geometry parameters for calculating attenuation and velocity dispersion.

Figure	Matrix	Inclusion	β	a (m)	b (m)
Fig. 3	WS rock 1	WS rock 2	0.2	-	0.01, 0.1, 1
Fig. 4	WS rock 1	WS rock 2	0.1, 0.3, 0.5, 0.8	-	0.5
Fig. 5	WS rock 1	WS rock 2	0.05, 0.15, 0.25, 0.4	0.5	-
Fig. 6	WS rock 2	WS rock 1	0.05, 0.1, 0.2, 0.3	-	1
Fig. 7	W/G/O-S rock 2	WS rock 1	0.25	-	0.5
Fig. 8	WS rock 1	GS rock 1/WS rock 2	0.15	-	0.4

WS denotes water-saturated, GS denotes gas-saturated, W/G/O-S denotes water/gas/oil saturated.

formula for the effective shear modulus in the classic elasticity model is given in Appendix C. In our calculation procedure the shear moduli of the matrix and inclusion and the inclusion concentration used in the elasticity model are all the same as those in the poroelastic model, and the value of the overall density is also the same as the effective density used in frequency-dependent velocity curves. The Poisson ratios of the matrix and inclusion used to calculate the effective shear moduli in the red and green lines are equal to the drained and undrained values, respectively. Fig. 3 (a) shows that for both of the two pore boundary situations discussed in Section 3.2 the drained S-wave velocity (red line) and undrained S-wave velocity (green line) are exactly equal to the low-frequency and high-frequency velocities of the poroelastic composite material, respectively. This indicates that with the increase of frequency, the double-porosity unit cell changes from a composite material having drained inclusions and drained matrix with no pore pressure difference to the same medium having undrained inclusions and undrained matrix with no fluid communication at the inclusion-matrix surface for both pore situations. The heterogeneous fluid-saturated medium behaves like an ordinary elastic composite at low-frequency and high-frequency limits. Both the low-frequency and high-frequency effective shear moduli can be calculated by means of Christensen and Lo (1979). In intermediate frequencies, the effective shear modulus increases with frequency and S-wave velocity lies between low-frequency and high-frequency values.

Next, we look at the differences between the two distinct pore boundary situations. Fig. 3 shows that the differences of the velocity dispersion and attenuation curves only occur at relatively low frequencies. Compared with the case of open pore situation, sealed pore situation has higher velocity and more attenuation at the relatively low frequencies. This is because the sealed pore situation at $r = b$ inhibits fluid flow and fluid pressure relaxation more than the open pore situation. Fig. 3(b) shows that there are two separate attenuation peaks for the case of the sealed pore situation, while there is only one peak for the case of the open pore situation. The maximum value of inverse quality factor for the case of sealed pore is smaller than that in the case of open pore.

Now, we consider the magnitude of attenuation in the double-porosity model. Fig. 4 plots the curves of inverse quality factor versus frequency for a double-porosity model with a fixed radius $b = 0.5$m but different inclusion concentrations. In this figure, physical properties of the matrix and the inclusion are the same as those used in Fig. 3. To quantify the attenuation for a wide range of inclusion concentration, we show the results for $\beta = 0.1$, 0.3, 0.5 and 0.8 (Table 3). $\beta = 0.1$ represents a small but not too dilute inclusion concentration, while $\beta = 0.8$ represents a very large inclusion concentrations. $\beta = 0.3$ and 0.5 represent two moderate inclusion concentrations. Fig. 4(a) and (b) give the results for the open pore situation and sealed pore situation, respectively. Fig. 4(a) shows that all open-pore inverse quality factor maximums are no more than 0.004 for various inclusion concentrations, while curves in Fig. 5(b) show that all sealed-pore inverse quality factor maximums are no more than 0.003. The measured level of attenuation for sedimentary rocks in seismic band lies within $0.01 < Q^{-1} < 0.1$ (Pride et al., 2004). Obviously, all the dilute, moderate and large inclusion concentrations show that the maximum values of the S-wave Q^{-1} are lower than 0.01 even if the inclusion stiffness is only 1% of the matrix. The softer inclusions with higher porosity than the matrix cause very weak attenuation. Moreover, attenuation characteristics for the two pore boundary situations are also very similar to each other. For example, at low frequencies the inverse quality factor scales with the first power of frequency ω, while at high frequencies the attenuation is proportional to $\omega^{-1/2}$.

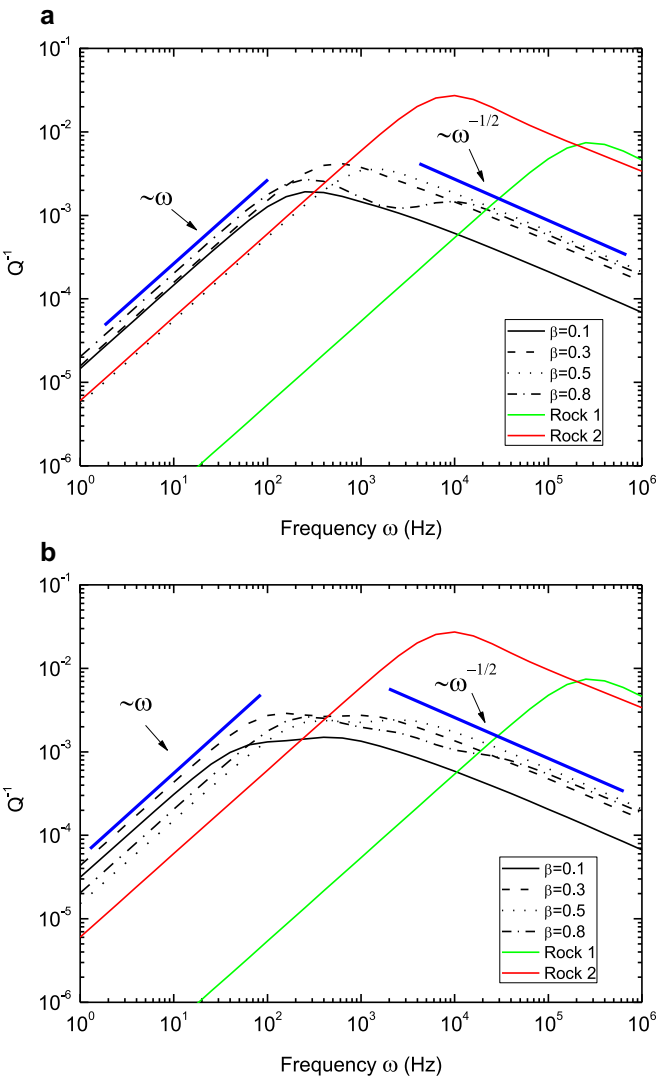

Fig. 4. Log-log plot of inverse quality factor Q^{-1} versus frequency ω of a double-porosity model with fixed unit cell radius $b = 0.5$m but with different inclusion concentrations of $\beta = 0.1, 0.3, 0.5$ and 0.8, respectively. (a) Q^{-1} for the open pore situation. (b) Q^{-1} for the sealed pore situation. The matrix is water-saturated rock 1, while the inclusion is water-saturated rock 2. The rock and fluid properties are given in Tables 1 and 2. The green and blue lines denote the Biot's global-flow S-wave attenuation in the matrix and the inclusion, respectively. Solid blue lines show asymptotic frequency dependencies of attenuation: ω at low frequencies and $\omega^{-1/2}$ at high frequencies. (For interpretation of the references to color in this figure legend, the reader is referred to the web version of this article).

Here, it is of great interest to compare the S-wave attenuation caused by mesoscopic WIFF with S-wave attenuation by the Biot global-flow mechanism (Biot, 1956a,b). The Biot attenuation is caused by viscous friction when pore fluid flows relative to the solid frame. The loss mechanism has a macroscopic nature and is the result of wavelength-scale fluid pressure equilibration between the peaks and troughs of conventional propagating wave. This induces a very small relative displacement between the solid frame and the fluid in S waves. The S-wave inverse quality factor for the Biot global flow can be expressed as

$$Q_{\text{Biot}}^{-1} = 2\frac{\text{Im}\left(\sqrt{\left(\rho - \rho_f^2/\tilde{\rho}\right)/\mu}\right)}{\text{Re}\left(\sqrt{\left(\rho - \rho_f^2/\tilde{\rho}\right)/\mu}\right)} \tag{58}$$

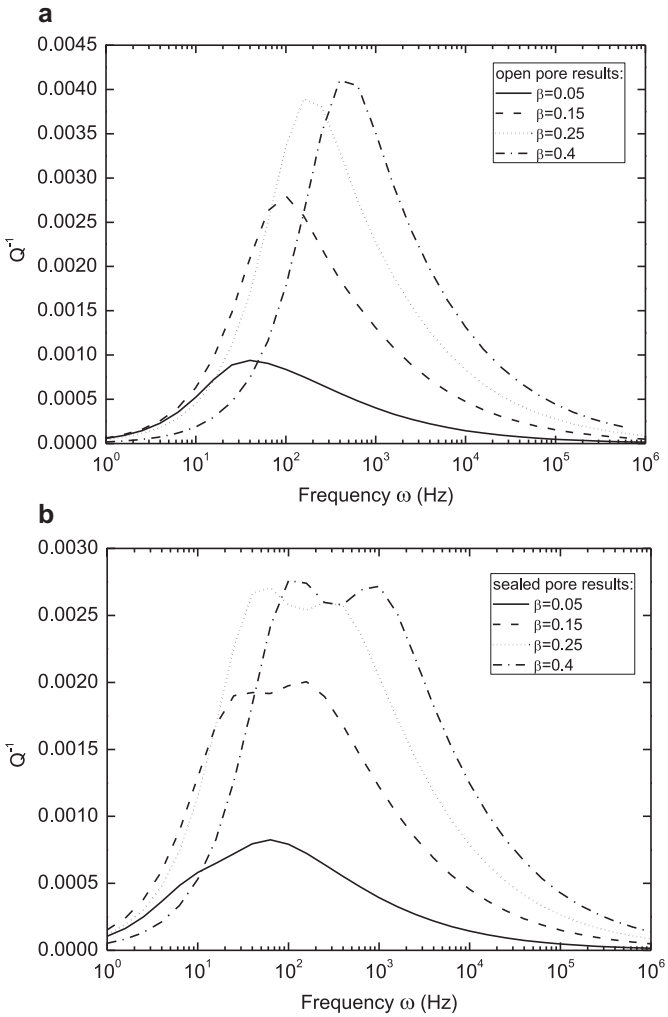

Fig. 5. Inverse quality factor Q^{-1} of a double-porosity model with fixed inclusion radius $a = 0.5$m but various inclusion concentrations of $\beta = 0.05, 0.15, 0.25$ and 0.4, respectively. (a) Q^{-1} for the open pore situation. (b) Q^{-1} for the sealed pore situation. The matrix is water-saturated rock 1, while the inclusion is water-saturated rock 2. The rock and fluid properties are given in Tables 1 and 2.

where

$$\rho = \phi\rho_f + (1-\phi)\rho_s\tilde{\rho} = \frac{i\eta}{\omega\kappa_D(\omega)}. \tag{59}$$

$\kappa_D(\omega)$ is the dynamic permeability. The dynamic permeability $\kappa_D(\omega)$ can be viewed as static permeability κ multiplied by its frequency correction factor (Johnson et al., 1987),

$$\kappa_D(\omega) = \kappa\left[\sqrt{1-\frac{i\omega}{2\omega_B}} - i\frac{\omega}{\omega_B}\right]^{-1}, \tag{60}$$

where

$$\omega_B = \frac{\phi\eta}{\rho_f\kappa\alpha_\infty} \tag{61}$$

is a so-called Biot characteristic frequency, α_∞ is the tortuosity. The attenuation caused by global flow is generally important in the range of ultrasonic frequencies, but it is not significant at the seismic frequency band. Keep in mind that the quasi-static flow discussed in the present paper is restricted to the long wavelength situation. To facilitate calculations, we select tortuosity $\alpha_\infty = \phi^{-2/3}$ (Liu et al., 2009). The green line and the red line in Fig. 4 represent the Biot S-wave attenuation in the rock 1 and rock 2, respectively. The comparison of attenuation curves in Fig. 4 shows

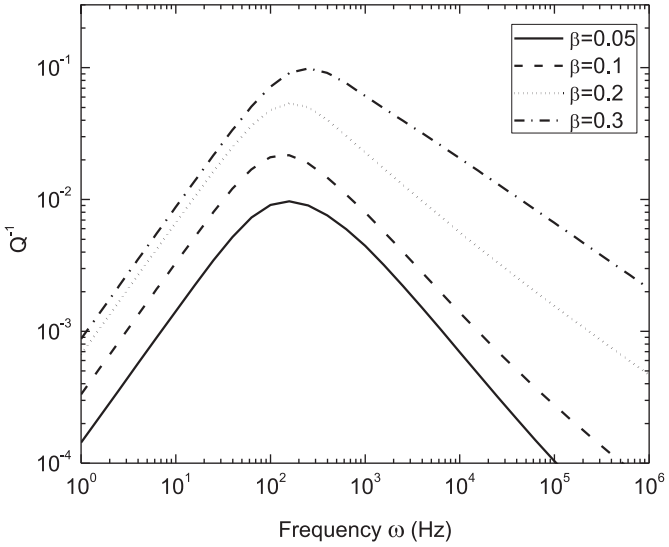

Fig. 6. Inverse quality factor Q^{-1} of a double-porosity model for open pore situation with fixed unit cell radius $b = 1$m but various inclusion concentrations of $\beta = 0.05, 0.1, 0.2$ and 0.3, respectively. The matrix is water-saturated rock 2 and the inclusion is water-saturated rock 1. The rock and fluid properties are given in Tables 1 and 2.

that the attenuation maximums caused by the mesoscopic WIFF are not larger than Biot's attenuation maximums (of the magnitude of 10^{-2}) although at frequencies below 10^3 values of attenuation caused by WIFF are nearly two orders of magnitude larger than the values of Biot attenuation in the rock 1.

Now, we consider the size-dependent characteristics of the S-wave relaxation frequency. Fig. 5 plots the double-porosity inverse quality factor Q^{-1} versus frequency for a fixed inclusion radius $a = 0.5$m but various inclusion concentrations of $\beta = 0.05$, 0.15, 0.25 and 0.4. The matrix and inclusion are also selected by water-saturated rock 1 and water-saturated rock 2, respectively (Table 3). Fig. 5(a) and (b) give the results for the open pore situation and sealed pore situation, respectively. They show that the attenuation maximum increases with the inclusion concentration and the relaxation frequency moves towards higher frequencies when the inclusion concentration increases (or when the unit cell radius decreases). Recall that Fig. 4 plots the curves of double-porosity inverse quality factor versus frequency with a fixed radius $b = 0.5$m but different inclusion concentrations. Fig. 4 shows that the relaxation frequencies move towards higher frequency when the inclusion diameter becomes bigger. Also recall that Fig. 3 plots the inverse quality factor versus frequency for a fixed inclusion concentration but various unit cell radii and inclusion radii. Fig. 3 shows that maximum attenuation position moves towards higher frequencies when the unit cell radius becomes smaller. Figs. 3–5 indicate that size-dependent characteristics of relaxation frequency are affected by both the radii of the unit cell and the inclusion.

Note that Figs. 3–5 only show the attenuation and dispersion curves for heterogeneous water-saturated porous solids which contain inclusions softer than the matrix. It is unknown whether a relatively stiffer inclusion imbedded in a soft matrix could cause a measured level of loss and whether the combined heterogeneities in both the solid frame and the fluid could enlarge the attenuation. Next, we use the three-phase model to calculate the attenuation and velocity dispersion for another two cases:

1. The inclusion has lower porosity and permeability and higher elastic moduli than the matrix, while the pore fluid is uniform (a double porosity structure having inclusions stiffer than the matrix).

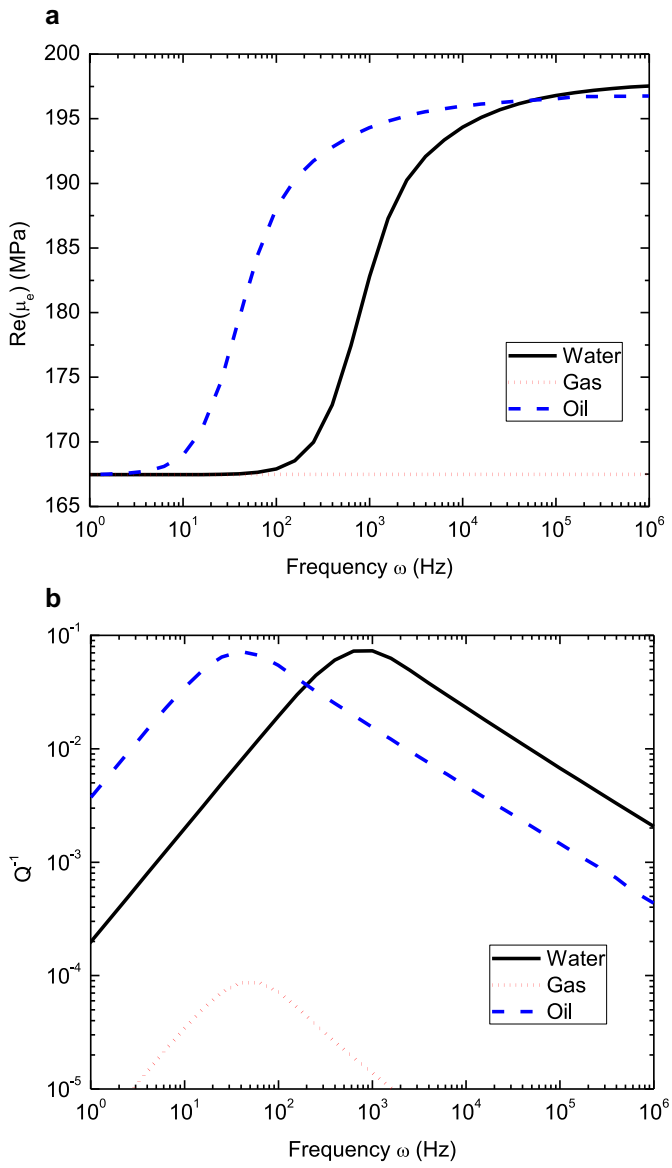

Fig. 7. Real part (a) and inverse quality factor (b) of the effective shear modulus for the open pore situation. The inclusion volume fraction is 0.25 and the unit cell radius is 0.5 m. The inclusion is always water-saturated rock 1, while the matrix is rock 2 which is saturated with three different kinds of fluids. The legend terms refer to the three saturation cases: water, gas, and oil. The rock and fluid properties are given in Tables 1 and 2.

2. The inclusion has a solid frame different from that of the matrix, and the pore fluid in the inclusion is also different from that in the matrix. (A combination model of heterogeneities in both the solid frame and the pore fluid.)

For simplicity, we only show the results for the open pore situation since the sealed pore situation has very similar properties.

Fig. 6 shows the inverse quality factor Q^{-1} of a double-porosity model with a stiff inclusion imbedded in a soft matrix for the open pore situation. The unit cell radius is $b = 1$m, and the various inclusion concentrations are $\beta = 0.05, 0.1, 0.2$ and 0.3. The figure shows that the maximum values of the inverse quality inverse Q^{-1} lie between 0.01-0.1 within seismic frequency $1 - 10^4$ Hz. Therefore, the case of a double-porosity model containing stiff inclusions imbedded in a soft matrix can explain the measured level of S-wave loss.

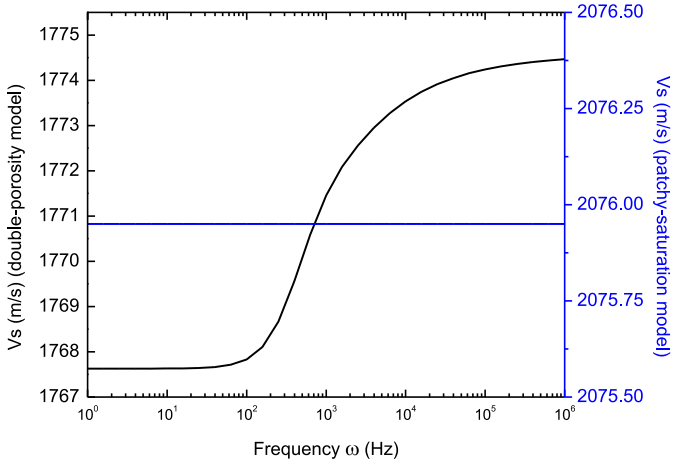

Fig. 8. Comparison of dispersion curves of S-wave phase velocity between a double-porosity model (black line) and a patchy-saturation model (blue line) with the same inclusion concentration $\beta = 0.15$ and the same radius $b = 0.4$m in the open pore situation. For the double-porosity model, the matrix is water-saturated rock 1 and the inclusion is water-saturated rock 2. For the patchy-saturation model, the matrix is water-saturated rock 1 and the inclusion is gas-saturated rock 1. The rock and fluid properties are given in Table 1 and 2. (For interpretation of the references to color in this figure legend, the reader is referred to the web version of this article).

Now, we look at the combined heterogeneities in solid frame and pore fluid. Fig. 7(a) and (b) show the real part and inverse quality factor of effective shear moduli for a combination model for open pore situation. The inclusion volume fraction is 0.25 and the unit cell radius is 0.5 m. The inclusion is always water-saturated rock 1, but the matrix is rock 2 which is saturated with three different kinds of fluids. The legend terms refer to the three saturation cases: water, gas, and oil. The rock and fluid properties are given in Tables 1 and 2. In this figure, we observe that real part of the shear modulus at the low-frequency limit is independent of the properties of the saturating fluid. However, for higher frequencies, the value of Re(μ_e) differs obviously when saturation fluid changes. The S-wave attenuation in the gas-saturated medium is very low and much lower than in the fully water-saturated and partially oil-saturated media. Moreover, at low frequencies equal to or lower than the relaxation frequencies in the oil-saturated medium, the S-wave attenuation is about one order of magnitude higher in the partially oil-saturated medium than in the fully water-saturated medium. Therefore, the pore fluids could cause significant effects on the dispersion and attenuation in the combined model.

Last, we consider the patchy-saturation model. In Fig. 8, we compare the S-wave velocity dispersion between a patchy-saturation model (blue line) and a double-porosity model (black line) with the same inclusion concentration $\beta = 0.15$ and the same radius $b = 0.4$m in the open pore situation. For the patchy-saturation model, the matrix is water-saturated rock 1 and the inclusion is gas-saturated rock 1. For the double-porosity model, the matrix is water-saturated rock 1 and inclusion is water-saturated rock 2. The velocity dispersion curves show that there is slight velocity dispersion in double-porosity model, whereas there is not any velocity dispersion in the patchy-saturation model at all. In Fig. 8, the calculated patchy-saturation effective shear modulus is 10GPa which is exactly identical to shear modulus of rock 1. We also calculate the effective shear modulus for other sets of fluids (those are oil and gas, water and oil): the effective shear moduli are all equal to 10GPa. The non-dispersive shear modulus implies that there is no attenuation in the spherical patchy-saturation model.

5. Conclusions

The present paper has studied on the effects of mesoscopic wave-induced fluid flow on effective shear properties in a heterogeneous fluid-filled porous material with spherical inclusions. An exact analytical solution is presented for the effective shear modulus in a generalized self-consistent or three-phase model under the assumption that the diameter of a spherical unit cell is smaller than S-wave wavelength but larger than the size of pores. The analytical formula can be used to quantify the S-wave attenuation and velocity dispersion in a combined model with heterogeneity in both the solid frame and pore fluid. Neither the interface permeability (imperfect pore boundary at the inclusion-matrix interface) nor the capillary effect is taken into account.

The shear wave velocity and shear wave attenuation have been calculated for the double porosity model. It is shown that the phase velocity increases with frequency and then reaches a finite asymptotic value. By comparison with analytical solutions for the effective shear modulus in the classic three-phase elasticity model given by Christensen and Lo (1979), it is revealed that the unit cell in the low frequency range behaves as a poroelastic composite having a drained inclusion and drained matrix with no pore pressure difference, and that the poroelastic unit cell in the higher frequency range behaves as the same composite but having an undrained inclusion and undrained matrix with no fluid communication at the inclusion's surface. The frequency dependence of the derived shear modulus is entirely caused by mesoscopic WIFF with relaxation frequencies depending on the sizes of the unit cell and the inclusion.

It is well known that spherical inclusions can cause significant attenuation in P waves over the seismic frequency range not only for the double porosity model but also for the patchy saturation models (Ba et al, 2011; White, 1975). The P-wave attenuation peak occurs at a frequency at which the characteristic length of fluid diffusion (wavelength of slow P wave) approximately equals the size of the inclusion. In contrast, for the problem of S-wave attenuation, spherical inclusions can also cause significant attenuation over the seismic frequency band for double porosity, but spherical inclusions do not affect the shear dispersion characteristic of the fluid-filled host medium at all since the effective shear modulus is exactly identical to the drained shear modulus.

For the double porosity model, only the stiffer inclusions imbedded in a relatively softer matrix can cause sufficient S-wave attenuation in the seismic frequency band. Softer inclusions with higher porosity imbedded in a relatively stiff matrix cause only weak attenuation and slight dispersion in the spherical inclusion model. Even if the inclusion stiffness is only 1% of the matrix stiffness, the inverse quality factor maximum is lower than 0.01 for a wide range of the inclusion volume fractions.

Masson and Pride (2007, 2014) have used finite difference modeling to calculate the S-wave attenuation in a heterogeneous porous medium with an ellipsoidal inclusion. They show that an oblate spheroid inclusion can create more attenuation than the spherical inclusion. In the future, we plan to study the analytical solutions for the shear property of a heterogeneous porous medium with ellipsoidal inclusions, which will allow us to analyze the effects of meso-flow on S-wave attenuation and S-wave dispersion.

Moreover, we note that the fifth boundary condition at the interface ($r = b$) between the matrix and its surrounding effective medium remains an open issue. The present paper discusses two possible situations: (1) the open pore boundary ($p_f = 0$) which represents the expected value (average value) of the pore pressure in the self-consistent model, and (2) the sealed pore boundary ($w_r = 0$) which describes the actual displacement continuity at the pore-solid interface. Alternatively, the open pore situation models a thin high permeability layer in which the easy flow of fluid maintains the pore fluid pressure at its ambient value, while the sealed pore situation corresponds to the impermeable limiting situation in which no flow can occur across the pore-solid interface. The actual shear dispersion curves probably lie between the results predicted by the two situations. Numerical results show that the discrepancy in phase velocity dispersion curves between the two situations is small. We therefore believe the three-phase model can describe the effective shear properties accurately.

Acknowledgments

Yongjia Song thanks China Scholarship Council (CSC) for supporting his two-year visit at Northwestern University (NU). The work reported in this paper is supported by National Natural Science Foundation of China (Grants 41174110, 11372091).

Appendix A. Derivations of the change in fluid mass content and displacements

Suppose an $e^{-i\omega t}$ dependence. In a spherical coordinate system the diffusion equation of fluid mass content (5) can be expressed as

$$\left(\frac{\partial^2}{\partial r^2}+\frac{2}{r}\frac{\partial}{\partial r}+\frac{1}{r^2}\frac{\cos\theta}{\sin\theta}\frac{\partial}{\partial\theta}+\frac{1}{r^2}\frac{\partial^2}{\partial\theta^2}+\frac{1}{r^2}\frac{1}{\sin^2\theta}\frac{\partial^2}{\partial\varphi^2}+\frac{i\omega}{c}\right)\Delta m=0. \tag{A1}$$

Inserting Eq. (10) $\Delta m=\Delta M(r)\sin^2\theta\cos 2\varphi$ into Eq. (A1) leads to a spherical Bessel equation of the second order

$$\left[\frac{d^2}{d\varsigma^2}+\frac{2}{\varsigma}\frac{d}{d\varsigma}+\left(1-\frac{6}{\varsigma^2}\right)\right]\Delta M=0, \tag{A2}$$

where $\varsigma=kr$, $k=\sqrt{i\omega/c}$. So, the solutions for ΔM and Δm are

$$\Delta M=Ej_2(kr)+Fn_2(kr), \tag{A3}$$

and

$$\Delta m=[Ej_2(kr)+Fn_2(kr)]\sin^2\theta\cos 2\varphi, \tag{A4}$$

where j_2 and n_2 are two kinds of spherical Bessel function of the second order, E and F are constants to be determined.

Next, substituting displacements given by Eq. (7) into equilibrium Eq. (4) gives two coupled linear non-homogeneous ordinary differential equations

$$\frac{d^2U_r}{dr^2}+\frac{2}{r}\frac{dU_r}{dr}-\frac{8U_r}{r^2}+\frac{6U_\theta}{r^2}+\frac{1}{1-2\nu_u}\left(\frac{d^2U_r}{dr^2}+\frac{2}{r}\frac{dU_r}{dr}-\frac{2U_r}{r^2}-\frac{3dU_\theta}{dr}+\frac{3U_\theta}{r^2}\right)=\frac{\lambda_u-\lambda}{\alpha\mu\rho_f}\frac{d(\Delta M)}{dr}, \tag{A5}$$

and

$$\frac{d^2U_\theta}{dr^2}+\frac{2}{r}\frac{dU_\theta}{dr}-\frac{6U_\theta}{r^2}+\frac{4U_r}{r^2}+\frac{2}{1-2\nu_u}\left(\frac{1}{r}\frac{dU_r}{dr}+\frac{2U_r}{r^2}-\frac{3U_\theta}{r^2}\right)=\frac{\lambda_u-\lambda}{\alpha\mu\rho_f}\frac{2}{r}\Delta M, \tag{A6}$$

where ν_u is the undrained Poisson ratio. The Eqs. (A5) and (A6) can be noted as

$$\mathbf{\Gamma}_1(\mathbf{U})+\mathbf{\Gamma}_2(\mathbf{U})=\chi, \tag{A7}$$

where

$$\mathbf{\Gamma}_1 = \begin{pmatrix} \frac{d^2U_r}{dr^2} + \frac{2}{r}\frac{dU_r}{dr} - \frac{8U_r}{r^2} + \frac{6U_\theta}{r^2} \\ \frac{d^2U_\theta}{dr^2} + \frac{2}{r}\frac{dU_\theta}{dr} - \frac{6U_\theta}{r^2} + \frac{4U_r}{r^2} \end{pmatrix}, \tag{A8}$$

$$\mathbf{\Gamma}_2 = \frac{1}{1-2\nu_u}\begin{pmatrix} \frac{d^2U_r}{dr^2} + \frac{2}{r}\frac{dU_r}{dr} - \frac{2U_r}{r^2} - \frac{3dU_\theta}{dr} + \frac{3U_\theta}{r^2} \\ \frac{2}{r}\frac{dU_r}{dr} + \frac{4U_r}{r^2} - \frac{6U_\theta}{r^2} \end{pmatrix}, \tag{A9}$$

$$\chi = \frac{\lambda_u - \lambda}{\alpha\mu\rho_f}\begin{pmatrix} \frac{d(\Delta M)}{dr} \\ \frac{2}{r}\Delta M \end{pmatrix}. \tag{A10}$$

The general solutions for displacements in the homogeneous equation $\mathbf{\Gamma}_1+\mathbf{\Gamma}_2 = 0$ are shown in Christensen and Lo (1979). We write them as

$$U_r^0 = Ar - \frac{2\nu_u}{1-2\nu_u}Br^3 + \frac{5-4\nu_u}{2(1-2\nu_u)}\frac{C}{r^2} + \frac{D}{r^4}, \tag{A11}$$

and

$$U_\theta^0 = Ar - \frac{7-4\nu_u}{3(1-2\nu_u)}Br^3 + \frac{C}{r^2} - \frac{2}{3}\frac{D}{r^4}, \tag{A12}$$

where *A*, *B*, *C* and *D* are constants to be determined from the boundary conditions, and the superscript 0 denotes general solutions for homogeneous equations. So to obtain the general solutions for the non-homogeneous Eq. (A7), we just need to find one group of special solutions U_r^s and U_θ^s.

First, let's consider the equation $\mathbf{\Gamma}_1(\mathbf{U}^1) = \chi$ which can be rewritten as

$$\frac{d^2U_r^1}{dr^2} + \frac{2}{r}\frac{dU_r^1}{dr} - \frac{8U_r^1}{r^2} + \frac{6U_\theta^1}{r^2} = \frac{\lambda_u - \lambda}{\alpha\mu\rho_f}\frac{d(\Delta M)}{dr}, \tag{A13}$$

and

$$\frac{d^2U_\theta^1}{dr^2} + \frac{2}{r}\frac{dU_\theta^1}{dr} - \frac{6U_\theta^1}{r^2} + \frac{4U_r^1}{r^2} = \frac{\lambda_u - \lambda}{\alpha\mu\rho_f}\frac{2}{r}\Delta M. \tag{A14}$$

Eliminating the term U_θ^1 in (A13) and (A14) gives

$$\frac{\lambda_u - \lambda}{\alpha\mu\rho_f}\left[\frac{d^3(\Delta M)}{dr^3} + \frac{6}{r}\frac{d^2(\Delta M)}{dr^2} - \frac{12\Delta M}{r^3}\right] = \frac{d}{dr}\left\{\frac{1}{r}\frac{d}{dr}\left[\frac{1}{r^2}\frac{d}{dr}\left(\frac{1}{r}\frac{d}{dr}\left(r^4U_r^1\right)\right)\right]\right\} \tag{A15}$$

By using Eq. (A3), we have the special solutions for $\mathbf{U}^1$ are

$$U_r^1 = \frac{\lambda_u - \lambda}{\alpha\mu\rho_f}\frac{1}{5k}\{E[3j_3(kr) - 2j_1(kr)] + F[3n_3(kr) - 2n_1(kr)]\}, \tag{A16}$$

and

$$U_\theta^1 = -\frac{\lambda_u - \lambda}{\alpha\mu\rho_f}\frac{2}{5k}\{E[j_1(kr) + j_3(kr)] + F[n_1(kr) + n_3(kr)]\}. \tag{A17}$$

Next, let's consider the equation $\mathbf{\Gamma}_1(\mathbf{U}^2)+\mathbf{\Gamma}_2(\mathbf{U}^2) = -\mathbf{\Gamma}_2(\mathbf{U}^1)$, where

$$\mathbf{\Gamma}_2(\mathbf{U}^1) = \frac{1}{1-2\nu_u}\frac{1}{5k}\frac{\lambda_u - \lambda}{\alpha\mu\rho_f} \times \begin{pmatrix} E[2j_1(kr) - 3j_3(kr)] + F[2n_1(kr) - 3n_3(kr)] \\ 2E[j_1(kr) + j_3(kr)] + 2F[n_1(kr) + n_3(kr)] \end{pmatrix} \tag{A18}$$

By substitution, it is easy to test the special solutions for $\mathbf{U}^2$ are

$$U_r^2 = -\frac{1}{1-\nu_u}\frac{\lambda_u - \lambda}{\alpha\mu\rho_f}\frac{1}{10k}\{E[3j_3(kr) - 2j_1(kr)] + F[3n_3(kr) - 2n_1(kr)]\}, \tag{A19}$$

and

$$U_\theta^2 = \frac{1}{1-\nu_u}\frac{\lambda_u - \lambda}{\alpha\mu\rho_f}\frac{1}{5k}\{E[j_1(kr) + j_3(kr)] + F[n_1(kr) + n_3(kr)]\}. \tag{A20}$$

The special solutions for $\mathbf{U}^s$ in Eq. (A7) are the sum of $\mathbf{U}^1$ and $\mathbf{U}^2$:

$$U_r^s = \frac{\chi}{10k}\{E[3j_3(kr) - 2j_1(kr)] + F[3n_3(kr) - 2n_1(kr)]\}, \tag{A21}$$

$$U_\theta^s = -\frac{\chi}{5k}\{E[j_1(kr) + j_3(kr)] + F[n_1(kr) + n_3(kr)]\}, \tag{A22}$$

where $\chi = 2\frac{\lambda_u-\lambda}{\alpha H\rho_f}$, and where $H = \frac{2\mu(1-\nu_u)}{1-2\nu_u}$ is the P-wave modulus defined by (Biot, 1962).

Last, the general solutions for displacements in the non-homogeneous Eq. (A7) are

$$\mathbf{U} = \mathbf{U}^0 + \mathbf{U}^s \tag{A23}$$

Appendix B. Elements in 11 × 11matrix a

The choice of elements in matrix **a** is not unique due to the properties of matrix elementary transformation that could be applied in Eqs. (39)–(49). A group of dimensionless elements are collected here.

For the case of open pore boundary ($p_f = 0$) at $r = b$,

$$a_{11} = 1, \quad a_{12} = 2\nu_{ui}, \quad a_{13} = (10ak_i)^{-1}\cdot[2j_1(k_ia) - 3j_3(k_ia)],$$
$$a_{14} = 1, \quad a_{15} = 2\nu_{um},$$

$$a_{16} = 2\nu_{um} - 2.5, \quad a_{17} = -1,$$
$$a_{18} = (10ak_m)^{-1}\cdot[2j_1(k_ma) - 3j_3(k_ma)],$$

$$a_{19} = (10ak_m)^{-1}\cdot[2n_1(k_ma) - 3n_3(k_ma)],$$

$$a_{21} = 1, \quad a_{22} = (7-4\nu_{ui})/3,$$
$$a_{23} = (5ak_i)^{-1}\cdot[j_1(k_ia) + j_3(k_ia)], \quad a_{24} = 1,$$

$$a_{25} = (7-4\nu_{um})/3, \quad a_{26} = 2\nu_{um} - 1,$$
$$a_{27} = 2/3, \quad a_{28} = (5ak_m)^{-1}\cdot[j_1(k_ma) + j_3(k_ma)],$$

$$a_{29} = (5ak_m)^{-1}\cdot[n_1(k_ma) + n_3(k_ia)]$$

$$a_{31} = 1, \quad a_{32} = -\nu_{ui},$$
$$a_{33} = \frac{1}{15}j_0(k_ia) + \frac{5}{21}j_2(k_ia) + \frac{6}{35}j_4(k_ia), \quad a_{34} = \mu_m/\mu_i,$$

$$a_{35}=-\nu_{um}\mu_m/\mu_i,\quad a_{36}=(5-\nu_{um})\mu_m/\mu_i,\quad a_{37}=4\mu_m/\mu_i,$$

$$a_{38}=\left[\frac{1}{15}j_0(k_ma)+\frac{5}{21}j_2(k_ma)+\frac{6}{35}j_4(k_ma)\right]\frac{\mu_m}{\mu_i},$$

$$a_{39}=\left[\frac{1}{15}n_0(k_ma)+\frac{5}{21}n_2(k_ma)+\frac{6}{35}n_4(k_ma)\right]\frac{\mu_m}{\mu_i}$$

$$a_{41}=1,\quad a_{42}=(7+2\nu_{ui})/3,$$
$$a_{43}=\frac{1}{15}j_0(k_ia)-\frac{1}{21}j_2(k_ia)-\frac{4}{35}j_4(k_ia),\quad a_{44}=\mu_m/\mu_i,$$

$$a_{45}=\frac{7+2\nu_{um}}{3}\frac{\mu_m}{\mu_i},\quad a_{46}=-(1+\nu_{um})\mu_m/\mu_i,\quad a_{47}=-\frac{8}{3}\frac{\mu_m}{\mu_i},$$

$$a_{48}=\left[\frac{1}{15}j_0(k_ma)-\frac{1}{21}j_2(k_ma)-\frac{4}{35}j_4(k_ma)\right]\frac{\mu_m}{\mu_i},$$

$$a_{49}=\left[\frac{1}{15}n_0(k_ma)-\frac{1}{21}n_2(k_ma)-\frac{4}{35}n_4(k_ma)\right]\frac{\mu_m}{\mu_i},$$

$$a_{52}=7(1-2\nu_{ui}),\quad a_{53}=-\frac{1}{2}\frac{H_{di}}{\lambda_{ui}-\lambda_i}j_2(k_ia),$$
$$a_{55}=7\frac{\lambda_{um}-\lambda_m}{\lambda_{ui}-\lambda_i}\frac{\alpha_i}{\alpha_m}(1-2\nu_{um}),$$

$$a_{56}=-3\frac{\lambda_{um}-\lambda_m}{\lambda_{ui}-\lambda_i}\frac{\alpha_i}{\alpha_m}(1-2\nu_{um}),$$
$$a_{58}=-\frac{1}{2}\frac{H_{dm}}{\lambda_{ui}-\lambda_i}\frac{\alpha_i}{\alpha_m}j_2(k_ma),$$

$$a_{59}=-\frac{1}{2}\frac{H_{dm}}{\lambda_{ui}-\lambda_i}\frac{\alpha_i}{\alpha_m}n_2(k_ma),$$

$$a_{62}=14(1-2\nu_{ui}),\quad a_{63}=\frac{k_ia}{10}\frac{H_{di}}{\lambda_{ui}-\lambda_i}[3j_3(k_ia)-2j_1(k_ia)],$$

$$a_{65}=14\frac{\gamma_m}{\gamma_i}\frac{\lambda_{um}-\lambda_m}{\lambda_{ui}-\lambda_i}\frac{\alpha_i}{\alpha_m}(1-2\nu_{um}),$$
$$a_{66}=9\frac{\gamma_m}{\gamma_i}\frac{\lambda_{um}-\lambda_m}{\lambda_{ui}-\lambda_i}\frac{\alpha_i}{\alpha_m}(1-2\nu_{um}),$$
$$a_{68}=\frac{k_ma}{10}\frac{\gamma_m}{\gamma_i}\frac{H_{di}}{\lambda_{ui}-\lambda_i}\frac{\alpha_i}{\alpha_m}[3j_3(k_ma)-2j_1(k_ma)],$$

$$a_{69}=\frac{k_ma}{10}\frac{\gamma_m}{\gamma_i}\frac{H_{di}}{\lambda_{ui}-\lambda_i}\frac{\alpha_i}{\alpha_m}[3n_3(k_ma)-2n_1(k_ma)],$$

$$a_{74}=1,\quad a_{75}=2\nu_{um}\beta^{-\frac{2}{3}},\quad a_{76}=(2\nu_{um}-2.5)\beta,\quad a_{77}=-\beta^{\frac{5}{3}},$$

$$a_{78}=(10k_mb)^{-1}[2j_1(k_mb)-3j_3(k_mb)],$$
$$a_{79}=(10k_mb)^{-1}[2n_1(k_mb)-3n_3(k_mb)],$$

$$a_{7,10}=a_{7,11}=1,$$

$$a_{84}=1,\quad a_{85}=(7-4\nu_{um})\beta^{-\frac{2}{3}}/3,$$
$$a_{86}=(2\nu_{um}-1)\beta,\quad a_{87}=2\beta^{\frac{5}{3}}/3,$$

$$a_{88}=(5k_mb)^{-1}[j_1(k_mb)+j_3(k_mb)],$$

$$a_{89}=(5k_mb)^{-1}[n_1(k_mb)+n_3(k_mb)],\quad a_{8,10}=1,$$

$$a_{8,11}=-2/3,$$

$$a_{94}=1,\quad a_{95}=-\nu_{um}\beta^{-\frac{2}{3}},\quad a_{96}=(5-\nu_{um})\beta,\quad a_{97}=4\beta^{\frac{5}{3}},$$

$$a_{98}=\frac{1}{15}j_0(k_mb)+\frac{5}{21}j_2(k_mb)+\frac{6}{35}j_4(k_mb),$$

$$a_{99}=\frac{1}{15}n_0(k_mb)+\frac{5}{21}n_2(k_mb)+\frac{6}{35}n_4(k_mb),$$
$$a_{9,10}=\mu_e/\mu_m,\quad a_{9,11}=-4\mu_e/\mu_m,$$

$$a_{10,4}=1,\quad a_{10,5}=(7+2\nu_{um})\beta^{-\frac{2}{3}}/3,$$
$$a_{10,6}=-(1+\nu_{um})\beta,\quad a_{10,7}=-8\beta^{\frac{5}{3}}/3,$$
$$a_{10,8}=\frac{1}{15}j_0(k_mb)-\frac{1}{21}j_2(k_mb)-\frac{4}{35}j_4(k_mb),$$

$$a_{10,9}=\frac{1}{15}n_0(k_mb)-\frac{1}{21}n_2(k_mb)-\frac{4}{35}n_4(k_mb),$$
$$a_{10,10}=\mu_e/\mu_m,\quad a_{10,11}=\frac{8}{3}\frac{\mu_e}{\mu_m}.$$

$$a_{11,5}=7(1-2\nu_{um})\beta^{-\frac{2}{3}},\quad a_{11,6}=-3(1-2\nu_{um})\beta,$$
$$a_{11,8}=-\frac{1}{2}\frac{H_{dm}}{\lambda_{um}-\lambda_m}j_2(k_mb),$$

$$a_{11,9}=-\frac{1}{2}\frac{H_{dm}}{\lambda_{um}-\lambda_m}n_2(k_mb).$$

and remaining elements are identical to zero, where $\beta=(a/b)^3$.

For the case of sealed pore boundary ($w_r=0$) at $r=b$, only four components are different from these in case of open pore boundary. They are

$$a_{11,5}=14(1-2\nu_{um})\beta^{-\frac{2}{3}},\ a_{11,6}=9(1-2\nu_{um})\beta,$$

$$a_{11,8}=\frac{k_mb}{10}\frac{H_{dm}}{\lambda_{um}-\lambda_m}[3j_3(k_mb)-2j_1(k_mb)],$$

$$a_{11,9}=\frac{k_mb}{10}\frac{H_{dm}}{\lambda_{um}-\lambda_m}[3n_3(k_mb)-2n_1(k_mb)],$$

Appendix C. Effective shear modulus in the spherical three-phase elasticity model

The solution for the effective shear modulus μ_e in an elastic three-phase composite sphere is given by Christensen and Lo (1979). The solution can be written formally as

$$\bar{A}_1\left(\frac{\mu_e}{\mu_m}\right)^2+\bar{A}_2\frac{\mu_e}{\mu_m}+\bar{A}_3=0 \tag{C1}$$

where the constants $\bar{A}_1$, $\bar{A}_2$ and $\bar{A}_3$ are given by

$$\begin{aligned}\bar{A}_1=&\,8\left(\frac{\mu_i}{\mu_m}-1\right)(4-5\nu_m)\eta_1\beta^{10/3}\\&-2\left[63\left(\frac{\mu_i}{\mu_m}-1\right)\eta_2+2\eta_1\eta_3\right]\beta^{7/3}\\&+252\left(\frac{\mu_i}{\mu_m}-1\right)\eta_2\beta^{5/3}\\&-50\left(\frac{\mu_i}{\mu_m}-1\right)\left(7-12\nu_m+8\nu_m^2\right)\eta_2\beta\\&+4(7-10\nu_m)\eta_2\eta_3\end{aligned} \tag{C2}$$

$$\bar{A}_2 = -4\left(\frac{\mu_i}{\mu_m}-1\right)(1-5\nu_m)\eta_1\beta^{10/3} + 4\left[63\left(\frac{\mu_i}{\mu_m}-1\right)\eta_2+2\eta_1\eta_3\right]\beta^{7/3} - 504\left(\frac{\mu_i}{\mu_m}-1\right)\eta_2\beta^{5/3} + 150\left(\frac{\mu_i}{\mu_m}-1\right)(3-\nu_m)\nu_m\eta_2\beta + 3(15\nu_m-7)\eta_2\eta_3 \quad (C3)$$

$$\bar{A}_3 = 4\left(\frac{\mu_i}{\mu_m}-1\right)(5\nu_m-7)\eta_1\beta^{10/3} - 2\left[63\left(\frac{\mu_i}{\mu_m}-1\right)\eta_2+2\eta_1\eta_3\right]\beta^{7/3} + 252\left(\frac{\mu_i}{\mu_m}-1\right)\eta_2\beta^{5/3} + 25\left(\frac{\mu_i}{\mu_m}-1\right)\left(\nu_m^2-7\right)\eta_2\beta - (7+5\nu_m)\eta_2\eta_3 \quad (C4)$$

with

$$\eta_1 = \left(\frac{\mu_i}{\mu_m}-1\right)(49-50\nu_i\nu_m) + 35\left(\frac{\mu_i}{\mu_m}\right)(\nu_i-2\nu_m)+35(2\nu_i-\nu_m) \quad (C5)$$

$$\eta_2 = 5\nu_i\left(\frac{\mu_i}{\mu_m}-8\right)+7\left(\frac{\mu_i}{\mu_m}+4\right) \quad (C6)$$

$$\eta_3 = \left(\frac{\mu_i}{\mu_m}\right)(8-10\nu_m)+(7-5\nu_m) \quad (C7)$$

where ν_i and ν_m are the Poisson ratios of the inclusion and matrix, respectively. μ_i and μ_m are the shear moduli of the inclusion and matrix, respectively. β is the volume fraction of the inclusions, that is, $\beta=(a/b)^3$.

When $\mu_i=\mu_m$, μ_e satisfies the following equation:

$$B_1\left(\frac{\mu_e}{\mu_m}\right)^2+B_2\frac{\mu_e}{\mu_m}+B_3=0 \quad (C8)$$

where

$$B_1 = -4\eta_1\beta^{7/3}+4(7-10\nu_m)\eta_2 \quad (C9)$$

$$B_2 = 8\eta_1\beta^{7/3}+3(15\nu_m-7)\eta_2 \quad (C10)$$

$$B_3 = -4\eta_1\beta^{7/3}-(7+5\nu_m)\eta_2 \quad (C11)$$

and where η_1 and η_2 are

$$\eta_1 = 105(\nu_i-\nu_m) \quad (C12)$$

$$\eta_2 = 35(1-\nu_i) \quad (C13)$$

The solution for Eq. (C8) is

$$\left(\frac{\mu_e}{\mu_m}\right)_1 = 1 \quad (C14)$$

or

$$\left(\frac{\mu_e}{\mu_m}\right)_2 = \frac{4\eta_1\beta^{7/3}+(7+5\nu_m)\eta_2}{4\eta_1\beta^{7/3}-4(7-10\nu_m)\eta_2} \quad (C15)$$

But the only suitable solution for μ_e is

$$\mu_e = \mu_m \quad (C16)$$

because $(\frac{\mu_e}{\mu_m})_2<0$ if $\beta=0$ or if $\nu_i=\nu_m$.

This appendix corrects two misprints in the expressions given by Christensen and Lo (1979). Eqs. (C2) and (C6) are different from theirs.

References

Ba, J., Carcione, J.M., Nie, J.X., 2011. Biot-Rayleigh theory of wave propagation in double-porosity media. J. Geophys. Res. 116, B06202.

Ba, J., Cao, H., M, J., Gang Tang, C., Yan, X.-F., Sun, W.-t., Nie, Jian-xin, 2013. Multiscale rock-physics templates for gas detection in carbonate reservoirs. J. Appl. Geophys. 77–82.

Berryman, J.G., 1985. Scattering by a spherical inhomogeneity in a fluid-saturated porous medium. J. Math. Phys. 26 (6), 1408–1419.

Berryman, J.G., 2004. Poroelastic shear modulus dependence on pore-fluid properties arising in a model of thin isotropic layers. Geophys. J. Int. 157, 415–425.

Berryman, J.G., Berge, P.A., Bonner, B.P., 2002. Estimating rock porosity and fluid saturation using only seismic velocities. Geophysics 391–404.

Biot, M.A., 1941. General theory of three dimensional consolidation. J. App. Phys. 12 (2), 155–164.

Biot, M.A., 1956a. Theory of propagation of elastic waves in a fluid-saturated porous solid. I. low-frequency range. J. Acoust. Soc. Am. 28 (2), 168–178.

Biot, M.A., 1956b. Theory of propagation of elastic waves in a fluid-saturated porous solid. II. Higher frequency range. J. Acoust. Soc. Am. 28 (2), 179–191.

Biot, M.A., 1962. Mechanics of deformation and acoustic propagation in porous media. J. Appl. Phys. 33 (4), 1482–1498.

Bourbié, T., O. Coussy and B. Zinszner. Acoustics of porous media: Editions Technip. 1987.

Brajanovski, M., Gurevich, B., Schoenberg, M., 2005. A model for P-wave attenuation and dispersion in a porous medium permeated by aligned fractures. Geophys. J. Int. 163, 372–384.

Christensen, R.M., Lo., K.H., 1979. Solutions for effective shear properties in three phase sphere and cylinder models. J. Mech. Phys. Solids. 27, 315–330.

Ciz, R., Gurevich, B., 2005. Amplitude of Biot's slow wave scattered by a spherical inclusion in a fluid-saturated poroelastic medium. Geophys. J. Int. 160, 991–1005.

Ciz, R., Gurevich, B., Markov, M., 2006. Seismic attenuation due to wave-induced fluid flow in a porous rock with spherical heterogeneities. Geophys. J. Int. 165, 957–968.

Deresiewicz, H.A., Skalak, R., 1963. On uniqueness in dynamic poroelasticity. Bull. Seism. Soc. Am. 53, 783–788.

Dutta, N.C., Odé, H., 1979a. Attenuation and dispersion of compressional waves in fluid-filled porous rocks with partial gas saturation (White model)-Part I: Biot theory. Geophysics 44 (11), 1777–1788.

Dutta, N.C., Odé, H., 1979b. Attenuation and dispersion of compressional waves in fluid-filled porous rocks with partial gas saturation (White model)-Part II: results. Geophysics 44 (11), 1789–1805.

Dvorkin, J., Mavko, G., Nur, A., 1995. Squirt flow in fully saturated rocks. Geophysics 60 (1), 97–107.

Gurevich, B., Sadovnichaja, A.P., Lopatnikov, S.L., Shapiro, S.A., 1998. Scattering of a compressional wave in a poroelastic medium by an ellipsoidal inclusion. Geophys. J. Int. 133, 91–103.

Gurevich, B., Schoenberg, M., 1999. Interface conditions for Biot's equations of poroelasticity. J. Acoust. Soc. Am. 105 (5), 2585–2589.

Johnson, D.L., 2001. Theory of frequency dependent acoustics in patchy-saturated porous media. J. Acoust. Soc. Am. 110 (2), 682–694.

Johnson, D.L., J., Koplik, Dashen, R., 1987. Theory of dynamic permeability and tortuosity in fluid-saturated porous media. J. fluid Mech. 176, 379–402.

Jones, T.D., 1986. Pore fluids and frequency-dependent wave propagation in rocks. Geophysics 51 (10), 1939–1953.

Liu, X., Greenhalgh, S., Zhou, B., 2009. Scattering of plane transverse waves by spherical inclusions in a poroelastic medium. Geophys. J. Int. 176, 938–950.

Markova, G., Jarillo, R., Markov, M., Gurevich, B., 2014. Squirt flow influence on sonic log parameters. Geophys. J. Int. 196, 1082–1091.

Masson, Y.J., Pride, S.R., 2007. Poroelastic finite difference modeling of seismic attenuation and dispersion due to mesoscopic-scale heterogeneity. J. Geophys. Res. 112, B03204.

Masson, Y.J., Pride, S.R., 2014. On the correlation between material structure and seismic attenuation anisotropy in porous media. J. Geophys. Res.: Solid Earth 119 (4), 2848–2870.

Müller, T.M., Gurevich, B., 2004. One-dimensional random patchy saturation model for velocity and attenuation in porous rocks. Geophysics 69 (5), 1166–1172.

Müller, T.M., Gurevich, B., 2005. A first-order statistical smoothing approximation for the coherent wave field in random porous media. J. Acoust. Soc. Am. 117 (4), 1796–1805.

Müller, T.M., Gurevich, B., Lebedev, M., 2010. Seismic wave attenuation and dispersion resulting from wave-induced flow in porous rocks-a review. Geophysics 75 75A147–75A164.

Nagy, P.B., Blano, G., 1994. Experimental measurements of surface stiffness on water-saturated porous solids. J. Acoust. Soc. Am. 95 (2), 828–835.

Norris, A., 1993. Low-frequency dispersion and attenuation in partially saturated rocks. J. Acoust. Soc. Am. 94 (1), 359–370.

Pride, S.R., Berryman, J.G., 2003a. Linear dynamics of double-porosity dual-permeability materials. I. governing equations and acoustic attenuation. Phys. Rev. E 68 (3), 036603.

Pride, S.R., Berryman, J.G., 2003b. Linear dynamics of double-porosity dual-permeability materials. II. Fluid transport equations. Phys. Rev. E 68 (3), 036604.

Pride, S.R., Berryman, J.G., Harris, J.M., 2004. Seismic attenuation due to wave-induced flow. J. Geophys. Res. 109, B01201.

Qi, Q., Müller, T.M., Gurevich, B., Lopes, S., Lebedev, M., Caspari, E., 2014a. Quantifying the effect of capillarity on attenuation and dispersion in patchy-saturated rocks. Geophysics 79 (5), WB35–SB50.
Qi, Q., Müller, T.M., Rubino, J.G., 2014b. Seismic attenuation: effects of interfacial impedance on wave-induced pressure diffusion. Geophys. J. Int. 199, 1677–1681.
Qu, J., Cherkaoui, M., 2006. Fundamentals of Micromechanics of Solids. John Wiley & Sons, Inc.
Quintal, B., Steeb, H., Frehner, M., Schmalholz, S.M., 2011. Quasi-static finite-element modeling of seismic attenuation and dispersion due to wave-induced fluid flow in poroelastic media. J. Geophys. Res. 116, B01201.
Quintal, B., Steeb, H., Frehner, M., Schmalholz, S.M., Saenger, E.H., 2012. Pore fluid effects on S-wave attenuation caused by wave-induced fluid flow. Geophysics 77 (3), L13–L23.
Rice, J.R., Rudnicki, J.W., Simons, D.A., 1978. Deformation of spherical cavities and inclusions in fluid-infiltrated elastic materials. Int. J. Solids Struct. 14, 289–303.
Rubino, J.G., Ravazzoli, C.L., Santos, J.E., 2008. Equivalent viscoelastic solids for heterogeneous fluid-saturated porous rocks. Geophysics 74 (1), N1–N13.
Rudnicki, J.W., 1986. Fluid mass sources and point forces in linear elastic diffusive solids. Mech. Mater. 5, 383–393.
Sams, M.S., Neep, J.P., Worthington, M.H., King, M.S., 1997. The measurement of velocity dispersion and frequency-dependent intrinsic attenuation. Geophysics 62 (5), 1456–1464.
Song, Y., Hu, H., 2013. Effects of squirt-flow in cracks on drained bulk modulus of porous media. Chin. J. Theor. Appl. Mech. 45 (3), 395–405.
Tang, X.-M., Chen, X.-l., Xu, X.-k., 2012. A cracked porous medium elastic wave theory and its application to interpreting acoustic data from tight formations. Geophysics D245–D252.
Tisato, N., Quintal, B., 2013. Measurements of seismic attenuation and transient fluid pressure in partially saturated Berea sandstone: evidence of fluid flow on the mesoscopic scale. Geophys. J. Int. 195, 342–351.
Vogelaar, B., Smeulders, D., 2007. Extension of White's layered model to the full frequency range. Geophys. Prospect. 55, 685–695.
Vogelaar, B., Smeurders, D., Harris, J., 2010. Exact expression for the effective acoustics of patchy-saturated rocks. Geophysics 75 (4), N87–N96.
Wenzlau, F., Altmann, J.B., Müller, T.M., 2010. Anisotropic dispersion and attenuation due to wave-induced fluid flow: quasi-static finite element modeling in poroelastic solids. J. Geophys. Res. 115, B07204.
White, J.E., 1975. Computed seismic speeds and attenuation in rocks with partial gas saturation. Geophysics 40 (2), 224–232.
White, J.E., Mihailova, N., Lyakhovitsky, F., 1975. Low-frequency seismic waves in fluid-saturated layered rocks. Earth Phys. 10, 44–52.